

**Aging Behavior of Flexcast[®] Al-Mg Alloys with
Sc and Zr Additions**

by

Mojan Sohi

Bachelor of Applied Science, The University of British Columbia, 2010

A THESIS SUBMITTED IN PARTIAL FULFILLMENT
OF THE REQUIREMENTS FOR THE DEGREE OF

Master of Applied Science

in

THE FACULTY OF GRADUATE STUDIES

(Materials Engineering)

The University Of British Columbia

(Vancouver)

August 2012

© Mojan Sohi, 2012

Abstract

AA5xxx series Al alloys have presented great potential in recent decades for packaging and automotive applications. A recent further development of these alloys has been the addition of Sc and Zr. The presence of these elements is known to develop strengthening phases that also influence other metallurgical phenomena such as recovery and recrystallization. However, the low solubility of both Sc and Zr in Al requires high cooling rates during casting in order to attain a supersaturated solid solution which conventional DC casting is unable to achieve.

In this study, two Al- 3%Mg alloys, one Sc-free and the other containing 0.4% Sc were cast using the Flexcaster[®] available at the Novelis Global Technology Center (Kingston, Ontario). The Flexcaster[®] is a strip casting technology that transforms liquid aluminum into a directly rollable cast ingot that is not subject to scalping or homogenization processing. This technology is characterized by relatively high solidification and cooling rates.

Aging experiments were performed on as-cast and cold-rolled samples of the two alloys to study the evolution of strengthening phases and their impact on recovery and recrystallization. Both alloys were artificially aged following casting at 200, 300 and 400°C for times ranging from 30s to 72 hours. The alloys were characterized by hardness and tensile tests and electrical resistivity measurements as well as optical and electron microscopy in order to monitor the aging behavior of the alloys.

Results show enhanced strengthening in the Sc-containing alloy and superior high temperature microstructural stability in comparison to the Sc-free alloy as well as conventionally cast AlMgSc alloys.

Table of Contents

Abstract	ii
Table of Contents	iii
List of Tables	vi
List of Figures	vii
Glossary	x
Acknowledgments	xi
1 Introduction	1
2 Literature Review	5
2.1 Al-Sc Alloys	6
2.1.1 Precipitation of Al_3Sc Phase	6
2.1.2 Effect of Al_3Sc Phase on Microstructure Development and Mechanical Properties	8
2.2 Addition of Zr to AlSc Alloys	12
2.3 Addition of Sc and Zr to Al-Mg Alloys	15
2.3.1 Al-Mg-Sc System	15
2.3.2 Mechanical Properties of Al-Mg-Sc-(Zr) Alloys	16
2.4 Twin-Belt Casting	18
2.4.1 Casting Set-up and Characteristics: Direct Chill vs. Twin-Belt Casting	19

2.4.2	Cast Microstructure: DC vs. TBC	22
2.4.3	Mechanical Properties of AA5xxx Alloys: DC vs. TBC	23
3	Scope & Objective	25
4	Experimental Procedures	27
4.1	Casting	27
4.2	Cold Rolling	28
4.3	Heat Treatments	29
4.4	Hardness Testing	29
4.5	Tensile Testing	29
4.6	Electrical Resistivity	30
4.7	Microstructure Characterization	31
4.7.1	Optical Metallography	31
4.7.2	Scanning Electron Microscopy	31
4.7.3	Transmission Electron Microscopy	32
5	Results	33
5.1	Mechanical Testing	33
5.1.1	Microhardness Tests	33
5.1.2	Tensile Tests	34
5.2	Electrical Resistivity	41
5.3	Microstructural Characterization	43
5.3.1	Optical Metallography	43
5.3.2	Scanning Electron Microscopy	50
5.3.3	Transmission Electron Microscopy	55
6	Discussion	64
6.1	Tensile Properties and Correlation of Hardness and Tensile Tests	64
6.2	Correlation of Hardness and Resistivity Results	69
6.3	Estimation of the Volume Fraction and Critical Radius	82
6.4	Summary	93

7	Concluding Remarks and Perspectives	96
7.1	Conclusions	96
7.2	Future Recommendations	97
	Bibliography	100

List of Tables

Table 4.1	Compositional analysis of the base and the Sc-containing alloys (wt%).	28
Table 5.1	List of conditions for the base alloy for which Optical Metallography and TEM analysis were performed.	43
Table 5.2	List of conditions for the Sc alloy for which Optical Metallography and TEM analysis were performed.	44
Table 6.1	Resistivity coefficients (coeff) and resistivity contribution of each element (ρ_i) in the base alloy. ρ_i is determined by multiplying the wt% of each element by the corresponding coeff.	76
Table 6.2	Resistivity coefficients (coeff) and resistivity contribution of each element (ρ_i) in the Sc alloy. ρ_i is determined by multiplying the wt% of each element by the corresponding coeff.	76
Table 6.3	Values of constants used in equation 6.18	93

List of Figures

Figure 2.1	The Al-rich portion of Al-Sc binary phase diagram	7
Figure 2.2	Schematics of the DC casting process (a) and TBC (b).	20
Figure 2.3	Schematic of the TBC process.	21
Figure 5.1	The Vickers microhardness results versus aging time for the base and Sc alloys	35
Figure 5.2	The stress-strain curve for the AC and AC & aged samples for the Sc alloy.	38
Figure 5.3	The stress-strain curve for the as-rolled and CR & aged samples for the Sc alloy.	39
Figure 5.4	Uniaxial tensile test results for the Sc alloy in the AC and AC & aged conditions.	40
Figure 5.5	Uniaxial tensile test results for the Sc alloy in the as-rolled and CR & aged conditions.	40
Figure 5.6	The comparison of the Yield Strength (0.2%) of the CR and aged and the AC and aged conditions for the Sc alloy.	41
Figure 5.7	The electrical resistivity results versus aging time for the base and Sc alloys	42
Figure 5.8	Optical micrograph of the base and Sc alloys AC microstructure and grain structure obtained at near surface.	45
Figure 5.9	Optical micrograph of the AC base and Sc alloys aged at 300°C for 72Hrs	46
Figure 5.10	Through thickness grain structure of the base and Sc alloy in AR and CR and aged at 300°C.	48

Figure 5.11	Through thickness grain structure of the base and Sc alloy in AR and CR and aged at 400°C.	49
Figure 5.12	SEM Back Scatter Electron image of near surface AC microstructure of the base alloy.	51
Figure 5.13	SEM Back Scatter Electron image of near surface AC microstructure of the Sc alloy.	52
Figure 5.14	SEM Back Scatter Electron image of near surface AC microstructure of the Sc alloy.	53
Figure 5.15	SEM Back Scatter Electron image of near surface AC microstructure of the Sc alloy.	54
Figure 5.16	Bright field TEM images of AC microstructure of the (a) base and (b) Sc alloys and corresponding diffraction patterns. [110] zone axis.	56
Figure 5.17	Bright field TEM images AC ((a) and (b)) and CR ((c) and (d)) of the base alloy at various aging conditions . . .	58
Figure 5.18	Higher magnification bright field TEM image CR microstructure of the base of the base alloy after aging at 300°C for 72 hours.	59
Figure 5.19	Bright field TEM images AC ((a) and (b)) and CR ((c) and (d)) of the Sc alloy at selected aging conditions . . .	61
Figure 5.20	Bright field TEM image of the AC Sc alloy aged at 400°C for 72 hours.	62
Figure 5.21	Bright field TEM image of the CR Sc alloy aged at 400°C for 72 hours.	63
Figure 6.1	The correlation of the yield strength and corresponding hardness value for the Sc alloy. $R^2 = 0.84$	67
Figure 6.2	The correlation of the ultimate tensile strength and corresponding hardness value for the Sc alloy. $R^2 = 0.90$. . .	67
Figure 6.3	The estimated tensile and yield strengths of the Sc alloy for various aging times at 300°C.	68
Figure 6.4	The estimated tensile and yield strengths of the Sc alloy for various aging times at 400°C.	69

Figure 6.5	The Al rich corner of the Al-Mn phase diagram for an Al-3%Mg-0.5%Mn-0.1%Fe-0.05%Si (base alloy).	77
Figure 6.6	The change in hardness vs the change in resistivity during aging	79
Figure 6.7	The difference between the hardness/resistivity of Sc alloy and the base alloy vs. aging time at 300°C in the AC condition.	84
Figure 6.8	The difference between the hardness/resistivity of Sc alloy and the base alloy vs. aging time at 400°C in the AC condition.	85
Figure 6.9	The difference between the hardness of Sc alloy and the hardness of the base alloy up to the peak-aged condition at 300 and 400°C in the AC condition.	86
Figure 6.10	Schematic of interaction of a dislocation with a precipitate.	90
Figure 6.11	Estimated yield strength vs f of Al_3Sc precipitates. . . .	91
Figure 6.12	Estimated yield strength vs $f^{1/2}$ of Al_3Sc precipitates. . .	92

Glossary

TBC	Twin Belt Casting
DC	Direct Chill
NGTC	Novelis Global Technology Center
AC	As Cast
ICP	Inductively Coupled Plasma
CR	Cold Rolled
AR	As Rolled
SEM	Scanning Electron Microscopy
EDX	Energy-Dispersive X-ray Spectroscopy
TEM	Transmission Electron Microscopy
YS	Yield Strength

Acknowledgments

There are many people whose inspiration, support and encouragement made this work possible and for whom I would like to express my deepest gratitude and respect:

My supervisors, Dr. Warren Poole and Dr. Chad Sinclair from UBC and Dr. Nitin Singh from Novelis, for the support, guidance and direction they provided throughout this work.

Dr. Mark Gallerneault and Dr. David Lloyd from Novelis for the fascinating and fruitful discussions and for their guidance and enthusiasm.

Dr. Daehoon Kang from Novelis for the incredible patience and support he provided me with for the analysis and TEM work presented in this study.

Mr. Ed Luce and Mr. Don Steele also from Novelis for their help and amazing patience with me at Novelis and for sharing their extensive knowledge and expertise in processing and microstructure of Aluminum alloys.

My family and Jason for their endless love and care throughout my studies.

My friends Mary G. and WiLL for the fascinating discussions and laughs shared throughout the late nights of writing and working.

And finally I wish to also thank Novelis Inc. and the National Science and Engineering Research Council of Canada for providing funding support for this project.

Ce qui embellit le désert, dit le petit prince, c'est, qu'il cache un puits quelque part...

Chapter 1

Introduction

Al-Mg (AA5xxx) alloys have undergone significant development in recent decades for use in packaging and automotive applications. These alloys show a combination of good strength, due to Mg in solid solution, good ductility and good corrosion resistance. A recent trend in further developing these alloys has been to add small amounts of Sc and/or Zr to additionally increase the strength of the alloy through precipitation hardening. This also has been found to have a beneficial effect on stabilization of the microstructure and in retention of strain-hardening at higher temperatures. The improved microstructural stability has mainly been attributed to the formation of nanometer size Al_3Sc or $Al_3(Sc, Zr)$ precipitates that inhibit the recovery and recrystallization of deformed microstructure [1]. Additions of Sc to Al-Mg alloys have therefore been shown to improve the strength of these alloys without a severe loss of ductility by combining the solid solution strengthening of Mg with the precipitation hardening of the Al_3Sc precipitates. The strengthening potency of the precipitates depends on the

size, volume fraction and spatial distribution. The beneficial properties of AlMgSc alloys however, are limited by the low solubility of Sc in Al. This limits the volume fraction of precipitates to less than 1%. As a result, further strengthening in these alloys is achieved by a combination of strain hardening, achieved by cold rolling the supersaturated alloy prior to aging and Al_3Sc precipitation hardening produced by final heat treatment. During aging a degree of recovery occurs, reducing the dislocation density and hence softening the alloy and this is offset by Al_3Sc precipitation hardening. Optimizing the strength of AlMgSc alloys is critically dependent on the level of prior work and the subsequent aging treatment. Adding Zr to the alloys has also been shown to be an effective method for inhibiting precipitate coarsening at higher temperatures by forming $Al_3(Sc_x, Zr_{(1-x)})$ precipitates [2]. This makes AlMgScZr alloys appealing for applications in which strength retention is required at higher temperatures. Zr, similar to Sc, has a low solubility limit in Al [1].

The precipitation of fine (2-5nm) $Al_3(Sc, Zr)$ particles takes place during heat treatments at intermediate temperatures ($200^\circ C < T < 400^\circ C$) [1]. Therefore, in order to efficiently precipitate out small, uniformly distributed $Al_3(Sc, Zr)$ particles during annealing, a supersaturated solid solution of Sc and Zr would be required in the as-cast metal. This could be produced by a solution heat treatment or alternatively by employing a high cooling rate during casting. The dissolution of the $Al_3(Sc, Zr)$ phase, however, requires a high temperature (above $640^\circ C$, see Figure 2.1) and long time heat treatments. The latter option would, therefore, be more attractive as it would reduce the processing steps during alloy fabrication. Achieving a high su-

persaturation of solid solution in the as-cast structure is also economically beneficial. The current high cost of Sc (\$163/gram of 99.9%Sc or \$220/kg for an Al-2%Sc master alloy [3]), has limited the application of Al-Sc alloys to the aerospace industry and other specialized markets such as bicycle frames. Hence, it is desirable that the content of Sc in Al be reduced in order to lower the cost of the alloy while still retaining the high strength and recrystallization resistance provided by Al_3Sc precipitates. It is therefore crucial to efficiently utilize the Sc content added to the alloy to achieve the maximum strength enhancement possible.

Conventionally, Al alloys are cast through Direct Chill (DC) casting. Through this method, molten metal is poured into a mold which is cooled at a rate of 1-10 K/s [4]. Ingots typically 400-500mm thick are produced. This is followed by homogenization and/or hot rolling, commonly performed at 40% of the melting temperature of the alloy. In the case of AlMgScZr alloys, the slow cooling rate of DC casting, and the high thermomechanical treatment temperature used during processing, would result in the precipitation of the $Al_3(Sc, Zr)$ phase during casting and further coarsening of the precipitates during homogenization and hot rolling [2, 5–7]. These coarsened precipitates that are typically 20-100nm in size and are not effective in enhancing the strength of the alloy through precipitation hardening during further annealing treatments at intermediate temperatures [1].

This investigation focuses on the study of an AlMgScZr alloy, fabricated by Twin-Belt Casting (TBC). Twin-Belt casting is a continuous casting technology commonly used in production of AA1xxx series Al alloys but has however also been a proven casting technique for AA5xxx series alloys on a

laboratory scale. In TBC, molten metal is continuously passed in-between two water-cooled belts which solidify the metal at a rate of $\approx 100\text{K/s}$. In TBC, strips of less than 25mm are produced. These strips can be directly cold rolled after casting and require no homogenization or hot rolling treatment.

The high cooling rate of TBC and the elimination of the homogenization step, makes this casting process particularly attractive for producing Al-Mg alloys with Sc and Zr additions. In this work, the behavior of two TBC AlMgZr alloys is investigated: one Sc-free and the other with 0.4%Sc addition. Both alloys are studied in the as-cast and 80% cold rolled conditions at various aging times at 200, 300 and 400°C. The behavior of the alloys during aging was monitored through hardness tests and electrical resistivity measurements as well as optical and electron microscopy examinations.

Chapter 2 provides a review of previous work performed on the Al-Sc and AlMgSc alloys including microstructural and mechanical behavior. The scope and objectives of this work is reviewed in Chapter 3. The experimental methodologies used for characterizing the alloys is presented in Chapter 4. Chapters 5 and 6 present the results and discussion of the investigation respectively. Finally, Chapter 7 and provides concluding remarks and future recommendations.

Chapter 2

Literature Review

Al-Sc alloys have received considerable attention in the last few decades due to high strength and high temperature stability [1]. This chapter highlights the most prominent effects of Sc additions to Al alloys and in particular to Al-Mg alloys. First the basic properties of binary Al-Sc alloys will be discussed including microstructure and mechanical properties. Next the ternary Al-Sc-Zr system and its microstructural behavior will be presented. Then the addition of Sc and Zr to Al-Mg alloys and their effect on the mechanical properties of Al-Mg alloys will be discussed. Finally, an overview of the Twin Belt Casting (TBC) process will be presented as well as the comparison of the properties of alloys cast through TBC vs conventional Direct Chill (DC) casting. The advantages of TBC for alloys containing Sc and Zr will be also be discussed.

2.1 Al-Sc Alloys

The first reported literature on additions of Sc to Al appeared in a US patent in 1971 by Willey [8]. In this patent, the effect of small additions of Sc to pure Al as well as a number of AA1xxx, 5xxx and 7xxx series alloys was investigated. Willey concluded that additions of Sc to aluminum significantly enhanced the strength and markedly affected the recrystallization start temperature of Al alloys. In the following years, the majority of the literature available on Al-Sc alloys is from work performed in Russia during the 1980s where further investigations were made on the effect of combining Sc with other alloying additions in Al alloys [1]. It was shown that due to the low solubility of Sc in aluminum, high cooling rates were required in order to cause rapid solidification of the alloy to maintain supersaturation of Sc in solid solution during casting [9]. In this section, the effect of Sc additions on the microstructure and mechanical properties of Al alloys is discussed.

2.1.1 Precipitation of Al_3Sc Phase

As shown in the Al-Sc phase diagram (Figure 2.1) [10], the maximum solubility of Sc in Al is limited to 0.38wt.% (0.23at.%) and the eutectic temperature (660.0-660.1°C) is very close to melting point of the alloy. Above the maximum solubility point, fine coherent Al_3Sc precipitates form [1]. These precipitates have an $L1_2$ structure with the Sc atoms on the corners of the FCC lattice [1]. Al_3Sc precipitates have a density of 3.03g/cm³ and a lattice misfit strain of 1.36% [11] with the matrix at ambient temperature and 1.05% at 300 °C [2].

Al_3Sc precipitates have been most often reported as having a nearly

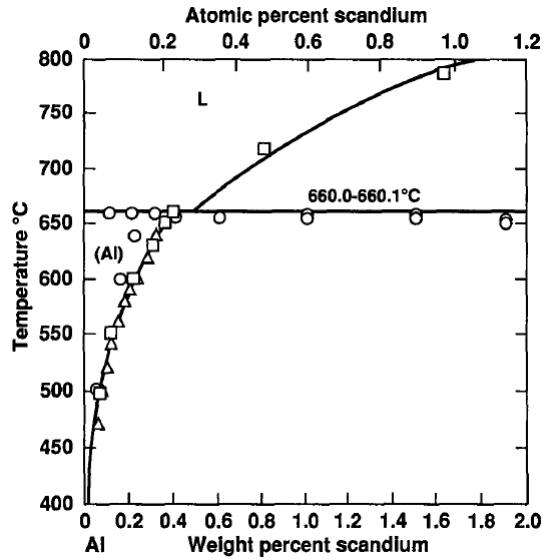


Figure 2.1: The Al-rich portion of Al-Sc binary phase diagram [10]. Springer and the original publisher/Metallurgical and Materials Transactions A, 23, 1992, 1947-1955, Homogeneous nucleation kinetics of Al_3Sc in a dilute Al-Sc alloy, Hyland R., Fig. 1, original copyright notice is given to the publication in which the material was originally published, by adding; with kind permission from Springer Science and Business Media.

spherical shape [1]. A number of other more complex morphologies however have also been observed [2, 11]. The precipitate morphology for alloys with Sc content lower than 0.2wt.% has been shown to be complex [11]. In this case, unstable cauliflower-shaped precipitates form initially and slowly transform to cuboidal morphologies with longer aging times and higher temperatures. Analysis of an Al-0.3%Sc alloy has shown multifaceted coherent Al_3Sc precipitates of radius 2-5nm forming during aging at temperatures between 300 and 450 °C [12]. The exact shape of these precipitates, which was also recently verified as the equilibrium shape, was determined both theoret-

ically and experimentally to be that of a Great Rhombicuboctahedron[12]. It has been shown that the Al_3Sc precipitates nucleate homogeneously at high supersaturations where the driving force for nucleation is high [10, 12]. However at high temperatures and low supersaturations, the precipitates tend to nucleate heterogeneously at dislocations and grain boundaries [12]. As mentioned previously the Al_3Sc precipitates have small lattice mismatch with Al and have shown slow coarsening rates in Al alloys which allows for remarkable stability at higher temperatures. The critical radius at which Al_3Sc precipitates have been shown to lose coherency is typically reported to be 40nm at a range of 0.1-0.3% Sc (at 400 °C) [1, 12, 13]. The slow coarsening rate of Al_3Sc precipitates has been attributed to the low diffusivity of Sc in Al. At 300°C, the diffusivity of Sc in Al is approximately $9 \times 10^{-20} m^2/s$ which is much lower than the diffusivity of Mg in Al at the same temperature ($\approx 10^{-16} m^2/s$) [14].

2.1.2 Effect of Al_3Sc Phase on Microstructure Development and Mechanical Properties

Grain Refinement

Grain refinement in casting of Al alloys has been shown to reduce casting defects such as shrinkage porosity and hot tearing and improve the mechanical properties of the alloy [1, 15, 16]. Al_3Sc particles have been shown to be particularly effective for grain refining if formed during or shortly after casting [1]. In this case, the Al_3Sc precipitates can act as effective nucleation sites for the $\alpha - Al$ phase provided the Sc content is hypereutectic [1]. Research has shown however that the eutectic composition of Sc is decreased

in presence of alloying additions such as Mg or Zr [1]. Simultaneous additions of Sc and Zr to Al alloys have been shown to be even more effective at grain refinement relative to Sc additions alone [1]. A study by Norman *et al.* showed an average grain size of $1000\mu\text{m}$ in a binary Al-0.2%Sc alloy and $80\mu\text{m}$ in a ternary Al-0.25%Sc-0.25%Zr alloy [17]. A similar study showed reduction of grain size with Sc and Zr additions to an Al-5%Mg alloy [18].

Recrystallization Resistance

As mentioned above the effects of Sc additions on the recrystallization start temperature of Al alloys was first reported in a patent by Willey [8]. In this patent it is reported that the recrystallization temperature of a cold-worked pure Al alloy is raised from 230°C to approximately 450°C with addition of 0.33wt.% Sc [8]. A similar effect was observed in alloys containing Mg and Mn as well as a 7075 series aluminum alloy. A study by Jones *et al.* on an Al-0.25%Sc alloy, reported a recrystallization start temperature of 500°C after aging for approximately 3 hours [19]. It has also been shown that the Al_3Sc dispersoids formed during homogenization or high temperature thermomechanical processing of the alloy inhibit recrystallization [1]. These dispersoids, typically 20-100nm in diameter, prevent rearrangement of the deformed microstructure through Zener drag. A study by Riddle *et al.* showed complete recrystallization resistance of an Al-0.2%Sc alloy upon annealing at 500°C [20]. The high temperature stability of the Al_3Sc phase also allows for retention of the deformed microstructure at high temperatures by pinning dislocations and preventing formation of recrystallized grains. This makes Sc additions particularly attractive for non-heat treat-

able wrought Al alloys [1]. In this case, the combination of precipitation hardening and strain hardening through cold-rolling allows for remarkable strengths and microstructural stability at higher temperatures. During aging a degree of recovery occurs which reduces the dislocation density in the alloy however this effect is offset by the hardening added from the Al_3Sc precipitates. This allows for high strength in the alloy without a severe loss of ductility.

Precipitation Hardening

It has long been noted that intermediate heat treatments of Al-Sc alloys (250–350 °C) produces fine coherent Al_3Sc precipitates typically 2-10nm in diameter which strengthen the alloy through precipitation hardening [1, 8]. It has been claimed that of all transition metals, Sc is the most potent strengthener in Al alloys, per atomic fraction [1]. The potency of the resultant Al_3Sc precipitates is dependent on the volume fraction, spatial distribution and size of the particles. As shown in the Al-Sc phase diagram however (Figure 2.1), the solubility of Sc in Al is quite low (0.38 wt%, at 660 °C). Therefore the volume fraction of precipitates formed during heat treatment is also low in comparison to more conventional precipitation hardening alloys. However, the effect of these precipitates is still significant. Marquis *et al.* investigated the effect of Al_3Sc precipitation in as-cast and aged binary Al-0.2%Sc and ternary Al-2%Mg-0.2%Sc alloys. An increase of approximately 900MPa in hardness was observed in both alloys during aging at 300°C [11].

Effect on Yield Strength - A number of studies have shown an increase in yield strength in Al-Sc alloys as a result of Al_3Sc precipitation [1, 8, 21–23]. As mentioned above the effect of these precipitates depends on their size and spatial distribution. These precipitates have been shown to impede dislocation motion, thereby increasing the yield strength of the alloy [1]. As a dislocation line encounters an array of precipitates, the dislocation begins to bow around the particles at a bowing angle of ϕ . As the applied stress is increased, the bowing angle decreases. At this stage, depending on the size and spacing (L) of the particles, the dislocation may shear the particle or bow around it. In the case of shearable particles, the dislocation will cut the precipitates and break free at a large breaking angle. In the case of non-shearable precipitates, the Orowan mechanism dominates, the breaking angle becomes zero and the dislocation forms a loop around the particles. The stress is given by [23]:

$$\sigma_{ppt} = \frac{MF}{bL} \quad (2.1)$$

where M is the Taylor factor, F is the force on the particle, b is the magnitude of the Burgers vector and L is the effective interparticle spacing.

A study on a binary Al-Sc study by Seidman *et al.* investigated effects of precipitate size on yield strength [21]. The shearable to non-shearable transition was found to occur at a precipitate average radius of about 2nm. A similar study by Fuller *et al.* on Al-Sc-Zr alloys showed the peak strength of the alloy is reached when the material is aged at 300 °C with the average particle radius of approximately 2nm [22]. A study by Fazeli *et al.* on

an Al2.8 wt.% Mg0.16 wt.% Sc, determined the shearable/non-shearable transition radius to be 3.7nm using a yield stress model to determine the critical [23].

Effect on Work Hardening - Fazeli *et al.* studied the effect of precipitates on the work hardening rate of an Al-2.8%Mg-0.16%Sc alloy through combined experiments and modeling [23]. The study was performed on alloys with under-aged, peak-aged and over-aged precipitates. It was found that the work hardening rate is enhanced for samples in the over-aged condition where the Al_3Sc precipitates are non-shearable [23]. As discussed previously, Orowan loops may form around non-shearable particles during particle-dislocation interactions. The formation of these loops causes higher internal stresses in the structure which results in higher work hardening rates. A similar study by Royset *et al.* on a binary Al-0.2%Sc alloy also showed higher work hardening rates for samples with over-aged precipitates [24]. In more recent work, Roumina *et al.* modeled the work hardening behavior of the same alloy studied by Fazeli *et al.* in the recovered stage and in the presence of Al_3Sc precipitates [25]. It was shown that the Al_3Sc precipitates strongly retain the deformed structure. A higher work hardening rate was observed when the average precipitate spacing was similar to the subgrain size in the microstructure [25].

2.2 Addition of Zr to AlSc Alloys

Several studies have been performed on the effect of Zr additions to Al-Sc alloys [1]. Similar to Sc, at high supersaturations, Zr forms an ordered FCC

$L1_2$ tri-aluminide, Al_3Zr , which has a high solubility in the Al_3Sc phase [1, 2]. Although the equilibrium structure of the Al_3Zr phase has been reported to be that of DO_{23} , it has been shown that if the Sc/Zr (wt%/wt%) ratio is higher than 1, then the $L1_2$ Al_3Sc phase forms with up to 50% of the Sc atoms substituted by Zr atoms [2]. When Zr is added, therefore, the precipitate phase is denoted as $Al_3(Sc_{(1-x)}, Zr_x)$ [1, 26]. Recent High Resolution Transmission Electron Microscopy (HRTEM) [26], atom-probe tomography [26] and small-angle X-ray scattering (SAXS) [27] investigations have shown that the $Al_3(Sc, Zr)$ phase consists of a core-shell structure with a Zr-rich shell and a Sc-rich core. This effect has been attributed to the lower diffusivity of Zr compared to that of Sc in Al. For example, at 300°C, the diffusivity of Sc is $9 \times 10^{-20} m^2/s$ while the Zr diffusivity is $6 \times 10^{-24} m^2/s$ [14]. This Zr shell results in a slow coarsening rate of the particles which allows for high temperature precipitate stability in the alloy and the retention of the strength added due to precipitation [1]. Knipling *et al.* compared precipitation of binary, Al-0.1%Sc, Al-0.1%Zr, and a ternary Al-0.1%Sc-0.1%Zr alloys [28]. It was found that the combined addition of Sc and Zr produced higher hardness than those of Sc and Zr alone. Upon annealing at 325 °C, a Zr-rich shell formed around the Al_3Sc precipitates which provided a higher peak hardness and retention of hardness for higher temperatures [28]. Similar behavior was observed in Al-0.06%Sc, Al-0.06%Zr, and Al-0.06%Sc-0.06%Zr [29]. A similar study by Fuller *et al.* on ternary $Al_3(Sc, Zr)$ alloys with various ratios of Sc/Zr showed a delay in coarsening of the precipitates with Zr present [22]. However no significant increase in peak hardness was observed with the addition of Zr.

As mentioned above, the addition of Zr has also been shown to improve the effects of Al_3Sc particles on grain refinement and recrystallization resistance of Al alloys. Knipling *et al.* reported equiaxed grains with average size of $50\mu m$ in the as-cast Al-Sc-Zr structure [28]. This grain size was much smaller than previously reported columnar grains larger than 1-2mm for as-cast binary Al-Sc and Al-Zr alloys [1, 11, 30]. Song *et al.* also reported a finer average grain size in alloys with increasing Zr content in comparison to a binary Al-0.39%Sc alloy [31]. The finer grain size in the ternary alloy can contribute to the higher hardness of the as-cast structure through Hall-Petch strengthening[32]. This study also reported that higher Zr contents contributed to higher yield strengths. It was discussed that the higher yield strength in presence of Zr may be attributed to the finer grains as well as the higher volume fraction of the precipitates in the ternary Al-Sc-Zr alloys. The alloy with the highest Zr content (0.68%) consisted of the highest volume fraction of precipitates and smallest average particle diameter [31]. Similarly, the addition of Zr has been shown to increase recrystallization resistance of the alloys [1, 26]. A comparison of an Al-0.4%Sc with that Al-0.4%Sc-0.15%Zr showed that the recrystallization start temperature, was increased from $520^{\circ}C$ in the binary alloy to $620^{\circ}C$ in the ternary alloy [1]. Similarly, in a study by Riddle *et al.*, recrystallization of an Al-0.2%Sc was retarded to $550^{\circ}C$ while a Al-0.12%Zr alloy showed immediate recrystallization. A ternary Al-0.12%Zr-0.2%Sc alloy however showed complete recrystallization resistance up to 24 hours at $590^{\circ}C$ [33].

2.3 Addition of Sc and Zr to Al-Mg Alloys

AA5xxx series aluminum alloys have undergone considerable development in the last few decades due to their high strength and potential in applications such as the beverage can (ex. AA5182 and AA5052) and automotive industries (ex. AA5754). The main alloying addition to these alloys is Mg (typically 2-5% Mg) which provides solid solution strengthening in the alloy (18.6MPa/wt% [34]). However the main strengthening component in these alloys is obtained through work hardening and grain size strengthening attained during cold deformation of the alloy. A recent trend in further development of these alloys has therefore been the addition of Sc. Small additions of Sc in Al-Mg alloys allows for a combination of solid solution strengthening from Mg and precipitation strengthening through the formation of Al_3Sc . However, as mentioned above, the Al_3Sc particles also inhibit recrystallization. Therefore the strength of the alloy obtained from strain hardening can be retained at higher temperatures and longer times.

2.3.1 Al-Mg-Sc System

It has been reported that the maximum solubility of Mg in Al is reduced in the presence of Sc from 16.8wt% at 450°C to 10.5 wt% at 447°C with the addition of 0.007at% Sc [11]. Studies on Al-Mg-Sc-(Zr) alloys have shown however that the precipitation of Al_3Sc or $Al_3(Sc, Zr)$ particles is not significantly influenced by the presence of Mg. Marquis *et al.* reported a slight change in the morphology of Al_3Sc precipitates in the presence of Mg where the precipitate morphology of an Al-2%Mg-0.2%Sc alloy was compared with that of a binary Al-0.3%Sc alloy [35]. It was found that the Al_3Sc particles

in the ternary alloy, exhibit a more spherical morphology compared to those found in a the binary alloy due to the reduction in interfacial free energy of the precipitates in the presence of Mg [35].

2.3.2 Mechanical Properties of Al-Mg-Sc-(Zr) Alloys

As mentioned above, the first reported work on addition of Sc to AA5xxx series alloys was by Willey in 1971 [8]. 0.3wt% addition of Sc was made to two alloys, one containing 1wt% and, another 5.3wt% Mg. Upon aging at 288 °C for 8 hours, the yield strength of of the alloy with 1% and 3%Mg increased from 43 to 288 and 147 to 368MPa, respectively due to the precipitation of Al_3Sc [8]. A similar study by Kaiser *et al.* on an as cast Al-6%Mg alloy with Sc additions of up to 0.6wt%, showed yield strengths as high as 325MPa (UTS 338MPa, 8%Elong.) with aging at 300 °C for 1 hour [36]. Fazeli *et al.* performed a combined modeling-experimental study on the effect of Al_3Sc precipitates on the yield strength of an Al2.8%Mg-0.16%Sc alloy [23]. In this study, a yield strength model [37] was combined with a precipitation model [38]. In the yield strength model, the maximum force required for a dislocation to pass a precipitate occurs at the shearable to non-shearable transition of the particle. Above a given size, the precipitates are non-shearable and therefore a passing dislocation will loop around the particle and the maximum force remains constant above this particle radius. It was found, that the peak strength due to Al_3Sc precipitation occurs at 300 °C after approximately 8 hours of aging [23].

There have also been several reports of the effect of Al_3Sc precipitates on the recrystallization resistance of Al-Mg-Sc alloys. Ocenasek *et al.* investi-

gated the comparison of an AA5754 with that of the same alloy with the addition of 0.25%Sc and 0.08%Zr [39]. It was found that the precipitation of $Al_3(Sc, Zr)$ inhibits recrystallization in this alloy up to 595 °C. It was also shown that the as-cast structure of the modified 5754 consisted of finer grains in comparison to that of the original 5754 alloy. Fuller *et al.* reported a similar finding for a modified 5754 alloy with 0.23%Sc and 0.22%Zr additions [40]. In this case first signs of recrystallization were observed in samples aged at 300 °C for 72hrs. Other studies have shown complete non-recrystallized structures in Al-Mg alloys with Sc additions [41].

The studies reviewed thus far in this section have investigated effects of Sc and Zr additions to Al-Mg alloys produced by Direct Chill (DC) casting. In these studies, DC cast ingots were produced through the traditional process of homogenization and/or hot rolling of the alloy at high temperatures (350-560 °C) following casting. As mentioned before, Sc and Zr have extremely low diffusivity in Al as well as very low solubility [1]. Therefore, if the ingot is not cooled rapidly during casting, $Al_3(Sc, Zr)$ particles could form in the cast structure. These particles would then coarsen rapidly during homogenization and/or hot rolling. This occurs since the dissolution of the $Al_3(Sc, Zr)$ phase is extremely difficult once it has been formed in the as-cast metal and would require high temperature (above 640°C, see Figure 2.1) and long time heat treatments. It is apparent, therefore, that an additional aging treatment would not result in further increase in strength after cold rolling since the precipitates would have already formed during casting and further annealing would only result in recovery in the alloy and further

coarsening of the particles. These coarse particles (50-100nm in size) may be sufficient for inhibiting recrystallization, but not sufficient for providing precipitation hardening. Precipitation strengthening could be provided by uniformly distributed precipitates of 2-5nm in size. Hence only one of the high temperature heat treatment or aging step would be required for the precipitation of the $Al_3(Sc, Zr)$ phase. This effect was evident in [2, 5–7]. It would therefore be desirable, that the starting as-cast structure be supersaturated with Sc and Zr. In that case, direct cold rolling and aging of the alloy would allow for precipitation hardening while retaining the recrystallization resistance of the alloy. In order to obtain a supersaturated solid solution however, high cooling rates would be required during casting to ensure rapid solidification of the slab and prevent formation of $Al_3(Sc, Zr)$ precipitates during casting. Studies on Al-Mg-Sc alloys cast through non-conventional methods such as Spray Forming [42] and Power Metallurgy [32] as well as semicontinuous DC casting [43], or DC casting utilizing cooling rates of above 100K/s [44] have shown superior strength levels due to the more rapid solidification rates used during alloy fabrication.

2.4 Twin-Belt Casting

A common continuous casting technique used for production of near net shape thin gauge aluminum alloys is Twin-Belt Casting (TBC). This process was first developed by Hazelett in 1919 and was installed in Alcan in 1959 [45, 46]. The Hazelett process was designed to allow a more efficient fabrication technique for production of thin-gauged aluminum sheets. However the width of the slabs fabricated through this process was limited. This process

was then further developed by Alcan in 1981 and was replaced by a TBC system able to cast wider strips [46]. This upgraded technology now resides in the Novelis Global Technology Center (NGTC) in Kingston, Ontario under the trade name of Flexcaster[®]. The Flexcaster[®] is mainly used for fabrication of fin, foil and container products (AA1xxx) [4]. However it has also been used to fabricate AA5xxx and AA6xxx alloys on a laboratory scale [4]. In this section, a comparison of TBC and DC casting conditions and microstructure will be presented followed by the mechanical properties of AA5xxx alloys cast through these fabrications routes.

2.4.1 Casting Set-up and Characteristics: Direct Chill vs. Twin-Belt Casting

TBC reduces the cost of sheet production by eliminating the scalping and homogenization steps which are otherwise required for ingots produced through traditional DC casting [45, 47]. DC cast ingots (typically 400-500mm thick) often require scalping, homogenization, hot rolling, cold rolling and then annealing. Continuous cast strips on the other hand (often less than 25mm thick) can be directly hot/cold rolled (Figure 2.2) [4, 45, 47]. Eliminating the scalping, homogenization, and hot rolling steps in TBC allows for significant reductions in the capital cost required for plant startup as well as maintenance and labor costs. Furthermore, TBC is a continuous casting process which allows for more efficient production in comparison to DC casting which requires a restart with fabrication of every ingot [48]. In addition, ingots cast through DC casting require significant reductions in size prior to further processing and final product development whereas TBC strips are

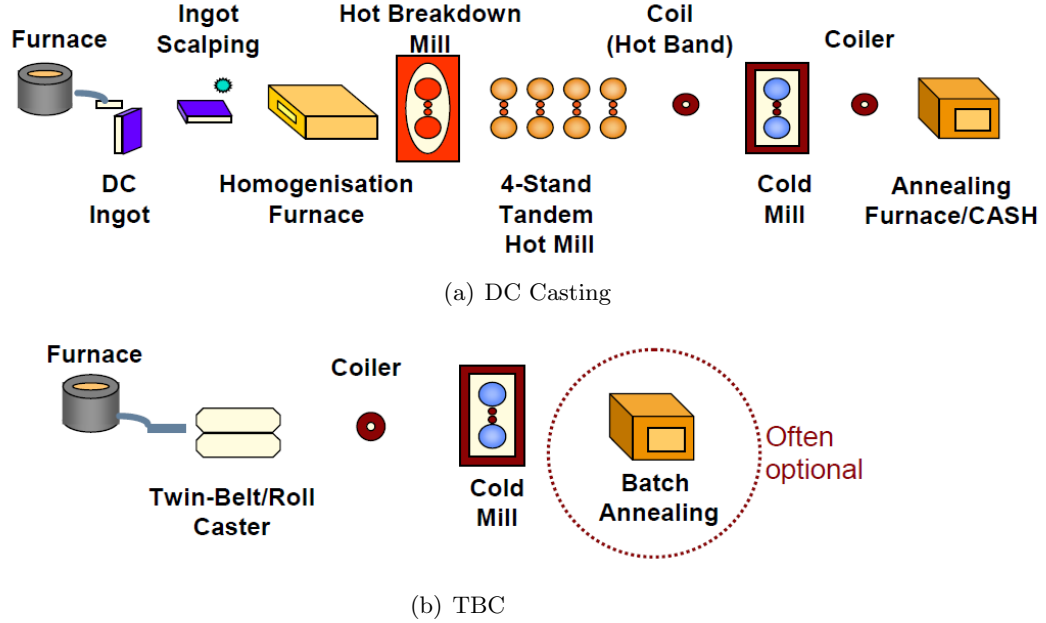


Figure 2.2: Schematics of the DC casting process (a) and TBC (b). As shown in the figures, the scalping, homogenization and hot rolling steps present in DC casting, are eliminated in TBC. ©Novelis Inc. by permission from [4].

much thinner and require less processing [47].

In TBC, molten aluminum is fed from a furnace into a cavity between two copper or steel belts which are continuously water cooled. The metal rapidly solidifies between the belts as it is passed through. The solidified strip coming out of the belt caster is then passed through pinch rolls (Figure 2.3). The strip can then be either cut as cast, coiled, cold rolled and/or annealed (Figure 2.2(b))[4].

TBC utilizes cooling rates ($\approx 100K/s$) that are significantly higher than those used in conventional DC casting ($1-10K/s$) [4, 47]. The rapid cooling rates used in TBC however also render the use of TBC more difficult for

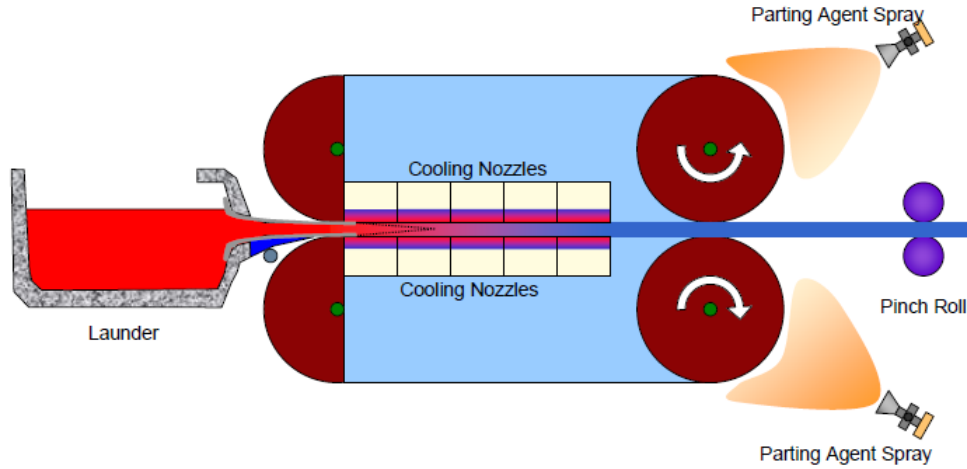


Figure 2.3: Schematic of the TBC process. ©Novelis Inc. by permission from [4].

casting alloys with a higher freezing range [48]. This is due to the solute partitioning which occurs during rapid solidification. In alloys with higher freezing range, the rapid cooling rate results in significant solute partitioning in the alloy which causes surface segregation and solute channeling resulting in poor sheet surface quality [47]. In alloys with low freezing range, solute partitioning is not significant due to the lower solute content. In order to reduce solute partitioning, higher control over the solidification rate is required. This can be attained through use of a parting agent which is continuously sprayed onto the belts in order to prevent the cast surface from sticking to the belt. Optimizing the pressure during casting as well as the use of pinch rolls on the solidified strip also allows for better control over the casting speed and solidification rate [48]. These improvements allow for casting of AA5xxx alloys with higher freezing range and therefore Mg content of 3%.

2.4.2 Cast Microstructure: DC vs. TBC

There are three main differences reported in the microstructure of DC cast material in comparison to TBC alloys:

Grain size - Grain sizes in the range of 40-50 μm for strip cast and 50-500 μm for ingot cast alloys have been reported [48–50]. The finer grain size in strip cast alloys can be attributed to the higher solidification rate which is used during casting. As mentioned above, cooling rates of approximately 100K/s may be reached in TBC while cooling rates of 1-10K/s are typical in ingot casting [4].

Constituent particle size and distribution - The high solidification rate in TBC can result in a different size and distribution of constituent particles in TBC relative to DC casting. In DC cast alloys, coarse constituent particles are typically formed during homogenization. In Al-Mg alloys in particular these particles are in the form of $Al_6(Fe, Mn)$ [48]. In TBC however, the strips are rapidly cooled and the homogenization step is eliminated. Therefore the constituent particles are much finer in TBC alloys in comparison to DC cast alloys since higher amounts of solute (Fe and Mn) remain in solid solution during casting [48, 50].

Solid solution content - As mentioned above the rapid solidification rate in TBC allows for supersaturation of solute in the as-cast structure of the alloy. Solute present in solid solution can interact with dislocations and therefore affect the recovery kinetics in the alloy during annealing. Previous

work on the comparison of ingot cast and TBC AA5754 has shown that the continuous cast alloy which was not homogenized showed slower recovery during annealing in comparison to the ingot cast alloy during the same heat treatments [51]. This characteristic makes TBC a particularly attractive option for fabricating Al-Mg alloys with Sc and Zr addition. As previously noted, the solubility of Sc in Al is very low (0.38% at the eutectic temperature). Therefore in order to obtain fine uniformly distributed $Al_3(Sc, Zr)$ precipitates, the Sc and Zr must be in solid solution prior to annealing at an intermediate temperature. If Sc and Zr are not in solid solution, then coarse primary particles of Sc and Zr will form which will be ineffective at enhancing the strength and microstructure of the alloy. Similarly if a homogenization step is used, Sc and Zr will precipitate out as $Al_3(Sc, Zr)$ and form coarse particles which will allow for inhibition of recrystallization however will be ineffective at enhancing the strength of the alloy through particle-dislocation interaction.

2.4.3 Mechanical Properties of AA5xxx Alloys: DC vs. TBC

Very few studies have been performed on the comparison of DC vs TBC 5xxx series alloys. Sarkar *et al.* compared the softening behavior of ingot cast and TBC AA5754 [51]. It was found that the continuous cast alloy which was directly cold rolled exhibited higher yield strength at all annealing times (at 200 °C) than the continuous cast alloy which was hot and cold rolled as well the ingot cast alloy which was fabricated through the traditional route of homogenization, hot rolling and cold rolling [51]. In a similar study by Zhao

et al. the behavior of Flexcast[®] Al-3%Mg alloy was compared with that of DC cast AA5182 and AA5052 alloys [50]. The Flexcast[®] alloy showed a higher yield strength relative to the DC cast alloys. The UTS of the TBC material was lower than that of the DC5182 however this was attributed to the lower Mg content of the TBC alloy [50].

As noted above, Sc and Zr form stable precipitates in the form of $Al_3(Sc, Zr)$ in Al alloys during intermediate temperature annealing which can provide significant precipitation hardening and recrystallization resistance. In Al-Mg alloys in particular, this effect can be combined with work hardening and solid solution strengthening of Mg and provide high strength and microstructure stability at high temperatures. However in order to efficiently use the strength which these precipitates provide, Sc and Zr must be in solid solution in the cast structure. This requires rapid cooling rates during solidification of the cast. The characteristics of TBC, as described above, therefore, make this process a particularly convenient fabrication route for production of Al-Mg alloys with small Sc and Zr additions. This work characterizes Al-Mg-Sc-Zr alloys cast through this method. The next chapter will outline the scope and objectives on this investigation.

Chapter 3

Scope & Objective

Based on the literature review discussed in the previous chapter, it is evident that the Al-Mg-Sc-Zr alloys provide great potential for high strength applications through retention of the deformed structure as well as precipitation hardening. However it is also apparent that in order to obtain the full potential of the mechanical properties of these alloys, a fabrication route which utilizes a high cooling rate must be used in order to attain a supersaturated solid solution in the as-cast structure. As discussed in the previous chapter, Twin-Belt Casting (TBC) provides such an option and has also never before been used for fabrication of Al alloys containing Sc. The objective of this work is to evaluate the feasibility of TBC for fabrication of Al-Mg alloys with Sc and Zr additions.

In order to achieve this objective, the aging response of two TBC Al-3%Mg alloys, one Sc-free and the other containing 0.4%Sc, was characterized in the as-cast and 80% cold-rolled conditions. The two alloys were heat treated at three intermediate temperatures: 200, 300 and 400 °C at times ranging from

30s to 72hours.

Two alloys were cast in order to determine the effect of Sc during aging in the Al-Mg alloy. Since the only difference between the two cast alloys was the level of Sc present, any variation in the response of the Sc-containing alloy from that of the Sc-free alloy will be assumed to be due to the 0.4%Sc added. The as-cast (AC) and 80% cold-rolled (CR) (10mm and 2mm thick) alloys were chosen in order to limit the complexity of the aging response. At intermediate cold deformations the precipitation kinetics of Sc and Mn in these alloys may have added further complications. The aging temperatures were chosen based on previous literature and the Al-Sc phase diagram. The response of the alloys were examined through Vickers microhardness tests, electrical resistivity measurements as well as optical and electron microscopy. Vickers hardness tests and electrical resistivity measurements both provide an indirect approach for examining precipitation in the alloy. However, Optical Metallography and Transmission Electron Microscopy (TEM) provided a direct method for observing microstructural evolution of the two alloys throughout the aging treatments.

This work will provide the knowledge necessary for assessing the suitability of Twin Belt Casting for the fabrication of Al-3%Mg alloys with Sc and Zr additions.

Chapter 4

Experimental Procedures

This chapter will outline the experimental procedures used for characterizing the two cast alloys. First, the casting procedure and parameters are described followed by the heat treatment procedures. Next, the equipment and parameters used for the mechanical testing and electrical resistivity are described. Finally the microstructure characterization of the alloys are outlined. All the described experiments and measurements were performed at Novelis Global Technology Center in Kingston, Ontario, Canada except the tensile tests performed on the as-cast (AC) samples. These uniaxial tensile tests on AC samples performed at UBC.

4.1 Casting

Two Al-3%Mg alloys were cast, one Sc-free and the other containing 0.4% Sc on the laboratory-scale Flexcaster[®] at NGTC. Both slabs were cast at 10mm gauge thickness. The Sc-free and the Sc-containing alloys were poured at 772°C and 767°C respectively. The Sc-free alloy was cast at 5.5m/min

Table 4.1: Compositional analysis of the base and the Sc-containing alloys (wt%).

Alloy	Mg	Mn	Sc	Zr	Fe	Si	Ti	V
Base	3.13	0.56	-	0.23	0.17	0.048	0.017	0.01
Sc	3.04	0.56	0.387	0.24	0.15	0.048	0.054	0.01

while the Sc-containing alloy was cast at 4m/min. The exit temperature for both casts was approximately 300°C. The slabs were air-cooled upon casting. In order to prevent precipitation in the as-cast Sc-containing slab, the slab was cut into smaller lengths and stacked with spacers in between each cut length to ensure faster cooling. Table 4.1 shows the chemical composition of the two as-cast alloys determined by inductively coupled plasma (ICP) analysis [52]. Throughout this work, the Sc-free alloy and the Sc-containing alloys will be referred to as the “Base” and “Sc” alloys respectively.

4.2 Cold Rolling

Both alloys were 80% cold rolled (CR) using the lab-scale rolling mill available at NGTC. The Sc-containing slab required light passes due to the high hardness of the material. This material was initially cold rolled by approximately 10% per pass. As the material became harder, reductions of approximately 4% per pass were used until a total reduction of 80% was obtained. However no large edge cracks were induced as a result of cold-rolling. The Sc-free slab was easily reduced to 2mm without requiring many light passes. This material was initially reduced by approximately 15% followed by 6-7% reductions per pass. Kerosene was used as lubricant during cold rolling.

4.3 Heat Treatments

Aging treatments were performed in air furnaces at times ranging between 15 minutes to 72 hours. Samples were inserted into furnaces preheated to the desired temperature. Samples were aged at 200, 300 and 400°C followed by quenching in water. Aging treatments for times shorter than 15 minutes were performed in a Nitrate salt bath (290 Draw Salt, APCO Industries Co. Ltd.) due to the high heating rate capability of the bath ($\approx 10^\circ\text{C/s}$).

4.4 Hardness Testing

Samples of 2.5cm x 2.5cm x 1cm (AC) and 2.5cm x 2.5cm x 2mm (AR) were prepared for microhardness tests. The cast surface of the samples was mechanically ground on 400 μm grit paper prior to testing. Vickers hardness testing was performed at each aging step on as cast as well as 80% CR samples. The Vickers hardness tests were performed using the Zwick Vickers Hardness Testing machine at 1kg load with a 10s dwell time in accordance to the ASTM E 384 standard. 3 hardness indents were used per test in order to obtain an average Vickers hardness number. The error associated with these measurements was $\pm 3\text{VHN}$.

4.5 Tensile Testing

Based on the hardness results for the 80% CR samples, peak-aged and over-aged conditions were determined at 300 and 400°C. Tensile tests were then performed on AC and aged, and CR and aged samples heat treated at these conditions as well as AC and as rolled (AR) samples. For the AC condition, the 10mm blank samples were machined down to 3.5mm with the center of

the sample at 1/4 thickness. Also, in the AC condition, only samples aged at 400°C, were tested and no samples aged at 300°C, were prepared due to the limited material available. It should also be noted that 2 samples were tested for each AC condition and 3 for the each CR condition. This was due to the limited AC material available for the Sc alloy. Tensile samples were prepared and tested in accordance to the ASTM E8 specifications. This specification dictated a strain rate of $10^{-3} s^{-1}$. At NGTC the 1169 - Instron 4202/5500R system was used for testing CR samples. In this case, an image correlation system was used for tracking the extension of gauge marks placed on tensile samples. The Instron 8872 model was used for testing AC samples at UBC. An axial clip-on extensometer was used for recording the elongation of the sample.

4.6 Electrical Resistivity

Similar to hardness tests, electrical resistivity measurements were performed at each aging step on as cast as well as 80% CR samples. Electrical resistivity measurements were performed using a Sigmatest D 2.068 at 60kHz for the AC samples and 240kHz frequency for the 80% CR samples. This apparatus was calibrated prior to each set of measurements performed for each aging step. The calibration was done using two standard Al samples as well as one Cu and one brass sample. For each aging step, the same sample was used for hardness and electrical resistivity measurements. The error associated with each electrical resistivity measurement was $\pm 0.3n\Omega \cdot m$

4.7 Microstructure Characterization

4.7.1 Optical Metallography

For Optical Metallography (OM), samples were hot mounted in Green PhenoCureTM and mechanically ground to $400\mu m$, polished to $3\mu m$ Diamond and $1\mu m$ Colloidal Silica and finally placed on Vibromat for 30 minutes. Microstructure and grain structure evaluations were performed optically using a Reitcher-Jung Polyvar-MET system. For microstructure analysis samples were etched for 10 seconds with 0.25% HF solution. A 2 minute Barkers anodizing process (2.5% HBF₄) was used for grain structure analysis.

4.7.2 Scanning Electron Microscopy

Scanning Electron Microscopy (SEM) and Energy-Dispersive X-ray spectroscopy (EDX) were performed using a Jeol JSM 5800 and the Philips XL30 FEG-SEM systems. Near surface and through thickness planes of the AC samples of both alloys were prepared and hot mounted in KonductoMet[®] and mechanically ground and polished to $3\mu m$. No etching was performed on the surfaces of the samples. These samples were analyzed in Back Scatter Electron (BSE) mode with the Jeol JSM 5800 at 20kV, 10mm working distance. For more detailed analysis, near surface planes of AC samples of the Sc alloy were electropolished and examined with the Philips XL30 FEG-SEM. Electropolishing was performed at 9V and $-25^{\circ}C$ for 60s in a 30% Nitric Acid, 70% Methanol electrolyte.

4.7.3 Transmission Electron Microscopy

Transmission Electron Microscopy (TEM) samples were prepared by mechanically grinding 3mm discs to approximately $100\mu m$ thick. Samples were then bulk electropolished using a 30% Nitric acid, 70% Methanol electrolyte, and 9V voltage at $-25^{\circ}C$. Each sample was electropolished for 60s. The analysis was performed using the Philips 420 system operating at 120kV. All TEM analyses were performed at NGTC.

Chapter 5

Results

This chapter describes the results of the mechanical and microstructural characterization performed on the base and Sc alloys as outlined in chapter 4. Vickers microhardness tests, and electrical resistivity measurements were used to monitor the response of the alloys during aging at 200, 300 and 400°C.

5.1 Mechanical Testing

Vickers Hardness tests were used to assess the mechanical response of the alloys during aging treatments. Tensile tests were performed only on the Sc alloy in order to determine the Yield Strength (σ_y) and ductility of the alloy for selected aging conditions.

5.1.1 Microhardness Tests

Figure 5.1 shows the Vickers hardness results of the base and Sc alloys during aging at 200, 300 and 400°C in the AC and CR conditions. In the AC

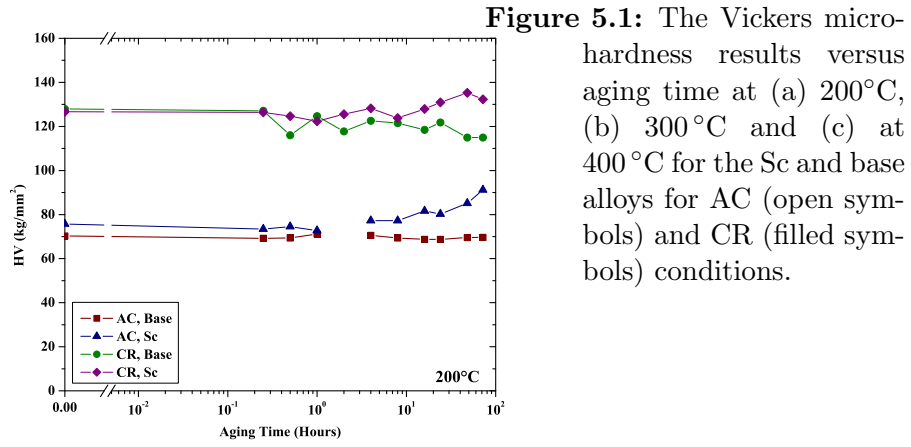
condition (0 aging time), the Sc alloy shows a slightly higher hardness (by $\approx 5\text{VHN}$) than the base alloy. Cold rolling caused an increase in hardness of approximately 45-50VHN in both alloys.

The base alloy does not show any increase in hardness at any of the temperatures in the AC case. In the CR case, a gradual decline in hardness is observed during aging. At 200°C , this response is very minimal, however as the temperature is increased, the decrease in hardness occurs more rapidly. As can be seen in Figure 5.1(c), at 400°C , the alloy has completely lost the hardness gained due to cold rolling after just 30 seconds of aging.

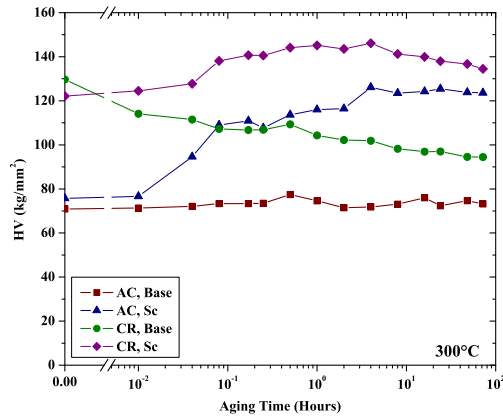
As shown in Figure 5.1(a), it can be observed that the hardness of the Sc alloy increased by about 15VHN in the AC case and 5VHN in the CR case after aging at 200°C for 72 hours. At 300°C , a stronger hardening response is observed (Figure 5.1(b)). The hardness of the Sc alloy has shown a maximum increase of 50 VHN in the AC cast and 24VHN in the CR case. At 400°C , a maximum hardness increase of 50VHN is reached much more rapidly, at 15 minutes in AC, and 30 seconds of aging in CR condition (Figure 5.1(c)).

5.1.2 Tensile Tests

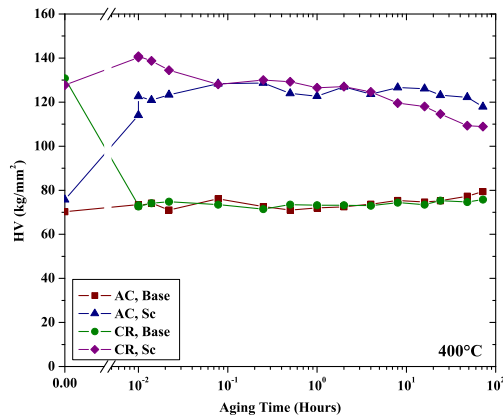
Due to limited amount of material available, tensile tests were not performed at all the aging steps used for hardness testing. Instead, based on the hardness results at 300 and 400°C , under-aged, peak-aged and over-aged conditions were determined for the Sc alloy and tensile tests were performed only at these conditions. The corresponding stress-strain curves are shown in



(a) Hardness versus aging time at 200 °C



(b) Hardness versus aging time at 300 °C



(c) Hardness versus aging times at 400 °C

Figures 5.2 and 5.3. It should be noted that, in the AC structure, porosity is very common and can cause early failure during a tensile test. In the present case, large variation was observed between the elongation at fracture of the AC samples for each condition. Two samples were tested for each condition and in each pair, one sample failed below 2% maximum elongation while the other reached maximum elongation higher than 9%. This early failure was attributed to the porosity which is typically present in AC structures. Since these samples were not well representative of the AC metal properties, only the curves for the samples with higher elongation are shown in Figure 5.2. It should also be noted that the data obtained from samples with early failure was not used in the analysis presented in the next chapter.

The CR samples, on the other hand, showed very little variation between the samples tested for each condition. The trend observed in the tensile results at 400°C in the CR condition is similar with those of the AC condition. Therefore, only the stress-strain curve for one sample is shown for each condition in Figure 5.3.

The serrations observed in the stress strain curves of the AC and CR samples (Figure 5.3) are due to the PortevinLe Chatelier (PLC) effect and are typical of Al-Mg alloys [53]. Detailed analysis of these serrations is beyond the scope of this work.

In both AC and CR tensile samples, a higher strength and uniform elongation was observed for aged samples in comparison to non-heat treated AC/CR samples. Figures 5.4 and 5.5 show a summary of the tensile test results for the AC and CR conditions respectively. In the AC condition, the tensile results for samples aged at 400°C, show a consistent trend relative

to the hardness data. The AC tensile results show an immediate increase in strength after aging at 400°C for 5 minutes. The uniform elongation of the AC samples was higher for aged samples relative to AC ones. The highest yield strength is observed after 15 minutes of aging at 400°C (Figure 5.4). In the CR condition, the highest yield strength is observed after 4 hours of aging at 300°C (384MPa) (Figure 5.5). This strength is 27MPa higher than that of the as-rolled condition and 23MPa higher than that of the 300°C-72 hours condition. Figure 5.6 shows a comparison of the yield strength of the aged CR and AC samples for the Sc alloy.

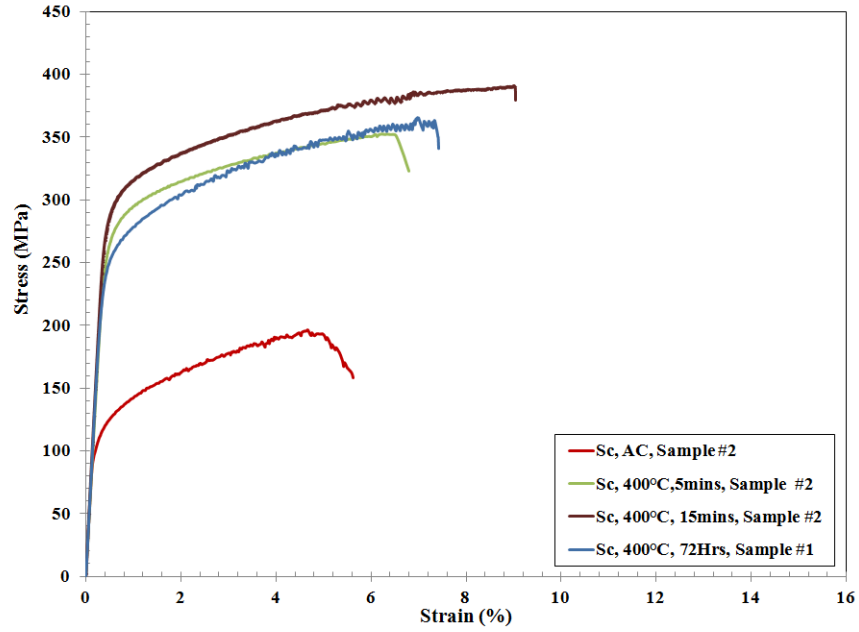


Figure 5.2: The stress-strain curve for the AC and AC & aged samples for the Sc alloy. Two samples were tested for each condition. Due to porosity in the AC structure, a large variation in the elongation at fracture between the samples in each pair was observed. In each pair, one sample failed with elongation less than 2% which was attributed to the porosity in the microstructure and therefore was not representative of the alloy properties. Therefore, only the curves for the samples which did not show early failure are shown here.

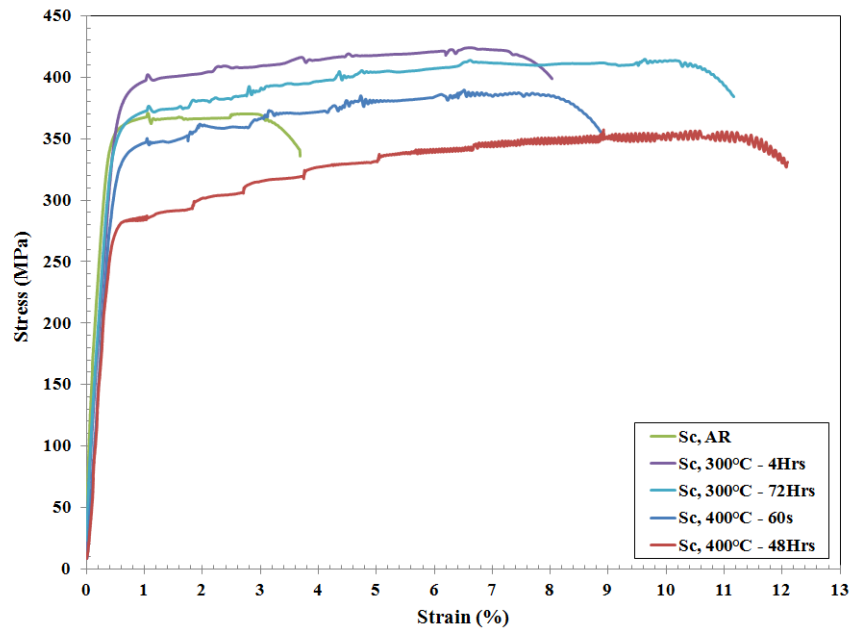


Figure 5.3: The stress-strain curve for the as-rolled and CR & aged samples for the Sc alloy. In this case, three samples were tested for each condition. Since there was little variation between the stress-strain curves for the three samples for each condition, the curve for only one of the samples for each condition is presented.

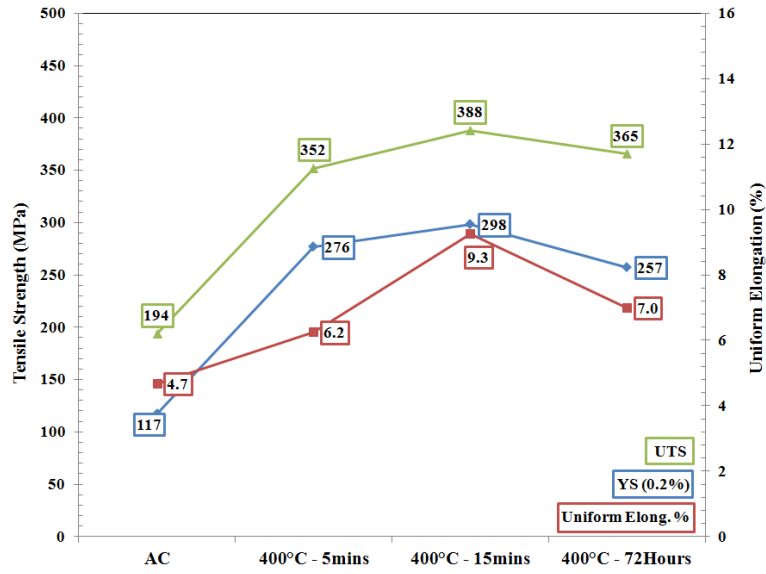


Figure 5.4: Uniaxial tensile test results for the Sc alloy in the AC and AC & aged conditions.

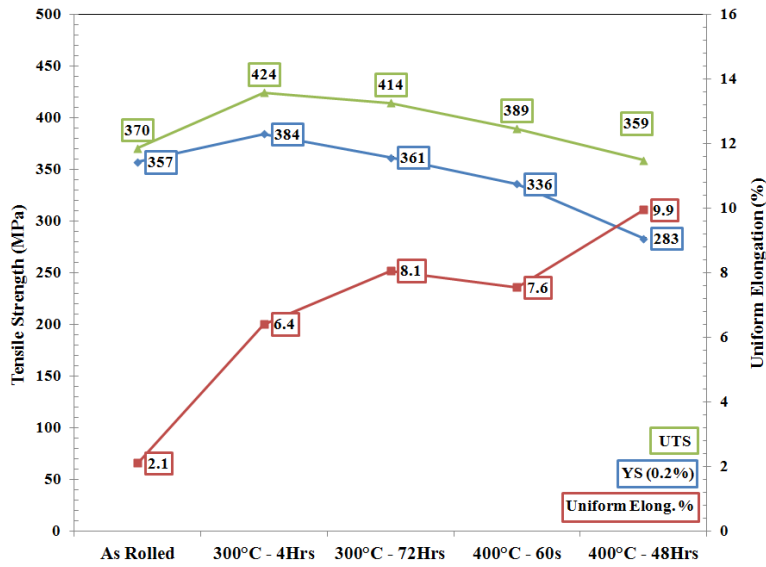


Figure 5.5: Uniaxial tensile test results for the Sc alloy in the as-rolled and CR & aged conditions.

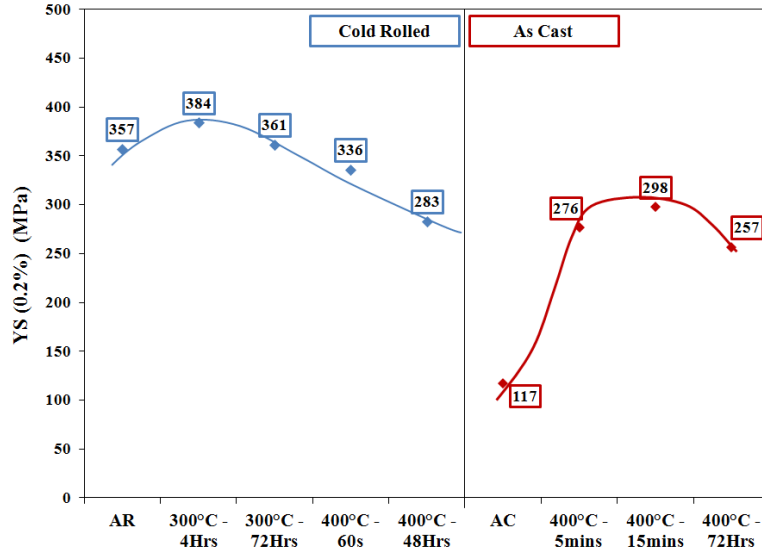
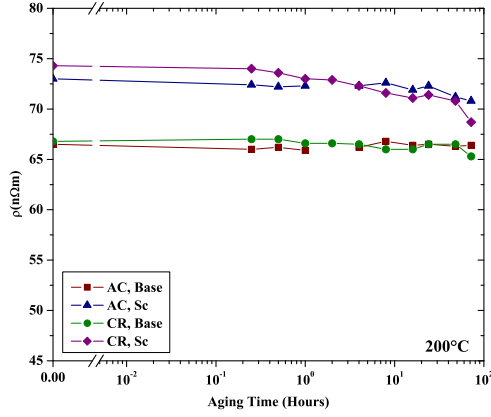


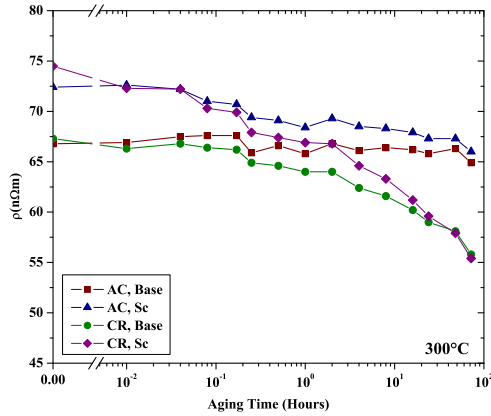
Figure 5.6: The comparison of the Yield Strength (0.2%) of the CR and aged and the AC and aged conditions for the Sc alloy.

5.2 Electrical Resistivity

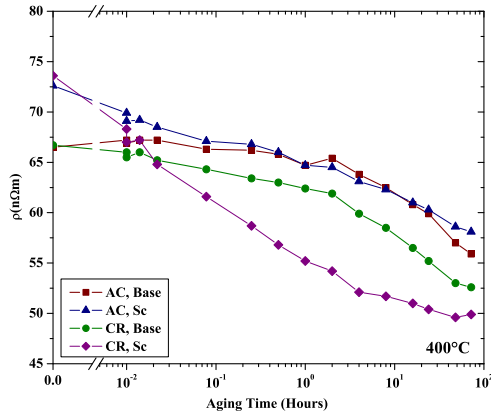
Figure 5.7 shows the electrical resistivity results for the base and Sc alloys for samples aged at 200, 300 and 400°C respectively. In all cases a gradual decrease in electrical resistivity was observed during aging treatments. This gradual decline in resistivity was progressively greater for higher temperatures. At 200°C the decrease in resistivity from the as-cast or as-rolled conditions to aged at 72 hours is approximately $4n\Omega \cdot m$ while for 300°C and 400°C this change was about 10 and $15n\Omega \cdot m$ respectively. For both alloys, a larger decline in resistivity was observed in the CR condition in comparison to the AC.



(a) Electrical Resistivity versus aging time at 200 °C



(b) Electrical Resistivity versus aging time at 300 °C



(c) Electrical Resistivity versus aging time at 400 °C

Figure 5.7: The electrical resistivity results versus aging time at (a) 200 °C, (b) 300 °C and (c) 400 °C for the Sc-containing alloy and the base alloy for the AC (open symbols) and CR (filled symbols) conditions.

5.3 Microstructural Characterization

5.3.1 Optical Metallography

Optical metallography was performed on as cast, as rolled as well as aged samples in order to assess the microstructure and grain structure of the two alloys. Similar to the tensile tests, the conditions for the samples were chosen based on the hardness results. Tables 5.1 and 5.2 summarize the conditions for which OM was performed for the base and Sc alloys respectively.

Table 5.1: List of conditions for the base alloy for which Optical Metallography and TEM analysis were performed.

Heat Treatment	Gauge	Aging Condition	Analysis Type
AC/AR	10mm/2mm	-	OM/TEM
300°C - 72Hrs	10mm	Over	OM/TEM
300°C - 4Hrs	2mm	Peak	OM
300°C - 72Hrs	2mm	Over	OM/TEM
400°C - 60s	10mm	Over	TEM
400°C - 30s	2mm	Over	TEM
400°C - 1Hrs	2mm	Over	OM
400°C - 72Hrs	2mm	Over	OM

AC Alloys - The AC base alloy consisted mainly of α -Al with constituents approximately $5\mu m$ or less in size evenly distributed throughout the structure (Figure 5.8(a)). The Sc alloy exhibited a similar structure but also contained large ($20\mu m$ or greater) primary intermetallics, throughout the structure (Figure 5.8(b)).

The grain structure of the two AC alloys showed an average grain size of approximately $200\mu m$ for the base alloy and $50\mu m$ for the Sc alloy respec-

Table 5.2: List of conditions for the Sc alloy for which Optical Metallography and TEM analysis were performed.

Heat Treatment	Gauge	Aging Condition	Analysis Type
AC/AR	10mm/2mm	-	OM/TEM
300°C - 24Hrs	10mm	Peak	TEM
300°C - 72Hrs	10mm	Over	OM
300°C - 4Hrs	2mm	Peak	OM/TEM
300°C - 72Hrs	2mm	Peak	OM
400°C - 15min	10mm	Peak	TEM
400°C - 60s	2mm	Peak	OM/TEM
400°C - 1Hrs	2mm	Over	OM
400°C - 72Hrs	2mm	Over	OM

tively (Figures 5.8(c) and 5.8(d)).

The microstructure and grain structure of both alloys exhibited similar features as the AC materials after aging at 300° for 72 hours (Figure 5.9).

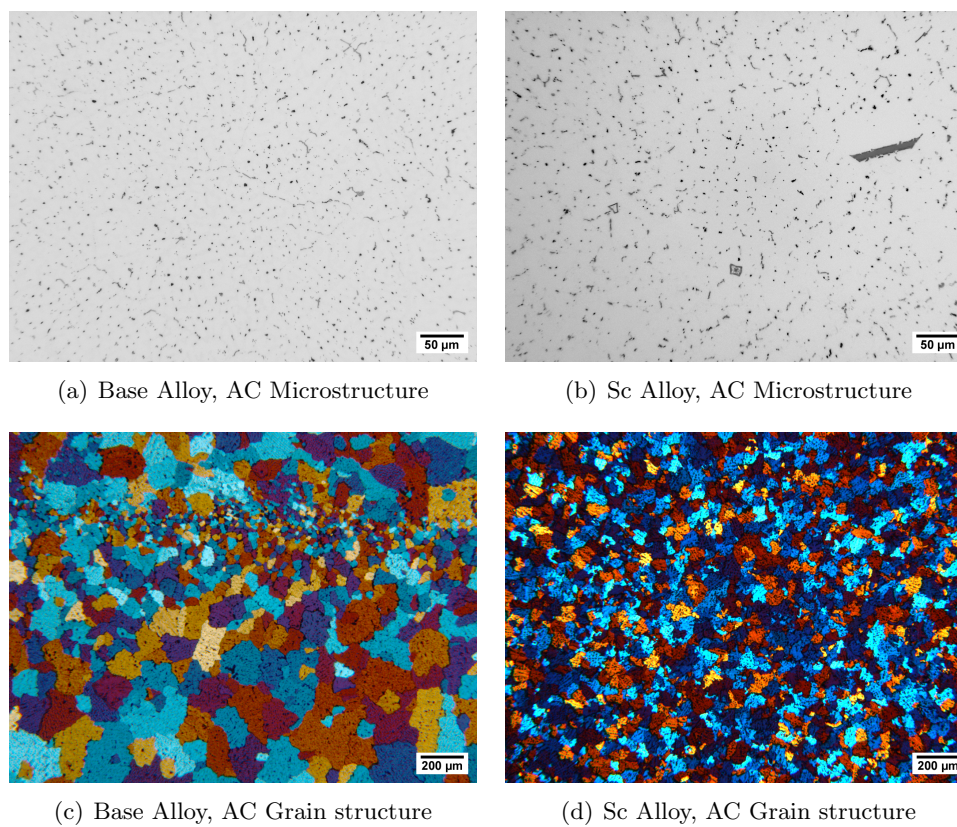


Figure 5.8: Optical micrograph of the base and Sc alloys AC microstructure and grain structure obtained at approximately 1mm from cast surface. (a), (c) Base, (b), (d) Sc.

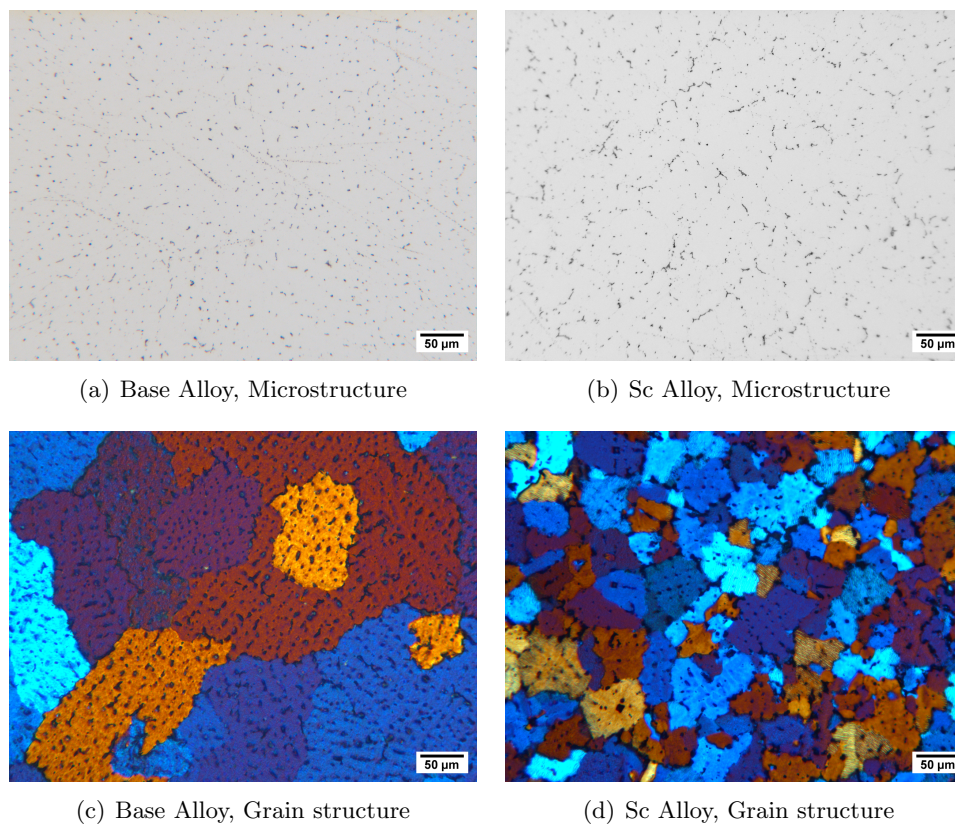


Figure 5.9: Optical micrograph of the AC base and Sc alloys aged at 300°C for 72Hrs (a) microstructure of base alloy, (c) grain structure of base alloy, (b) microstructure of Sc alloy and (d) grain structure of Sc alloy, obtained at approximately 1mm from cast surface.

CR Alloys - The as-rolled microstructure of alloy base also exhibited a smaller 'pancake' structure relative to the Sc alloy (Figures 5.10(a) and 5.10(d)). Examining the grain structure of the alloys after aging at 300°C for 72Hrs showed no sign of recrystallization in either alloy (Figure 5.10). After aging at 400°C, the base alloy showed complete recrystallization after 60 seconds of aging (Figure 5.11). The Sc alloy however remained unrecrystallized even after 72 hours at 400°C (Figure 5.11).

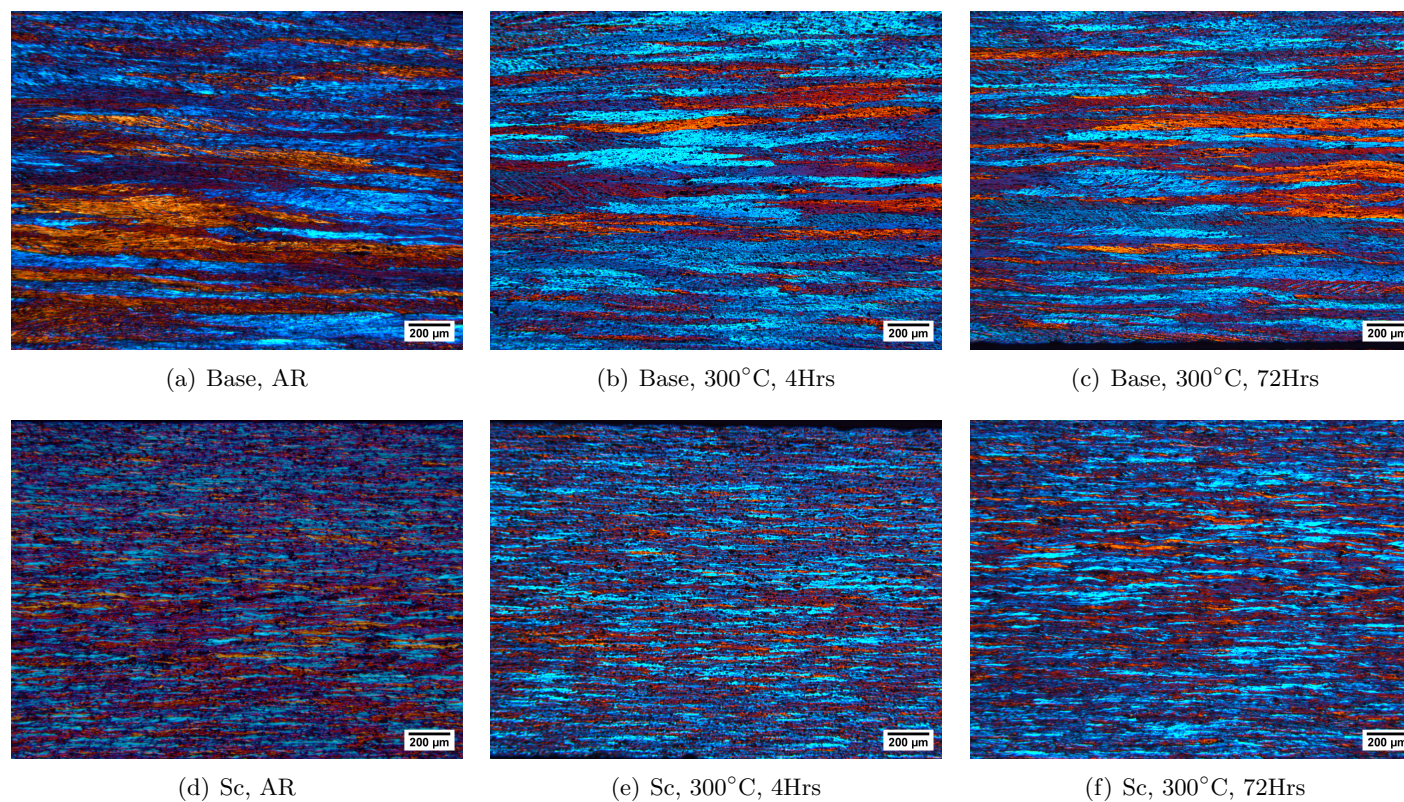


Figure 5.10: Through thickness optical micrographs of the base (top row) and Sc (bottom row) alloys in the AR ((a) ,(d)), CR and aged at 300°C for 4 hours ((b),(e)) and 72 hours ((c), (f)) conditions.

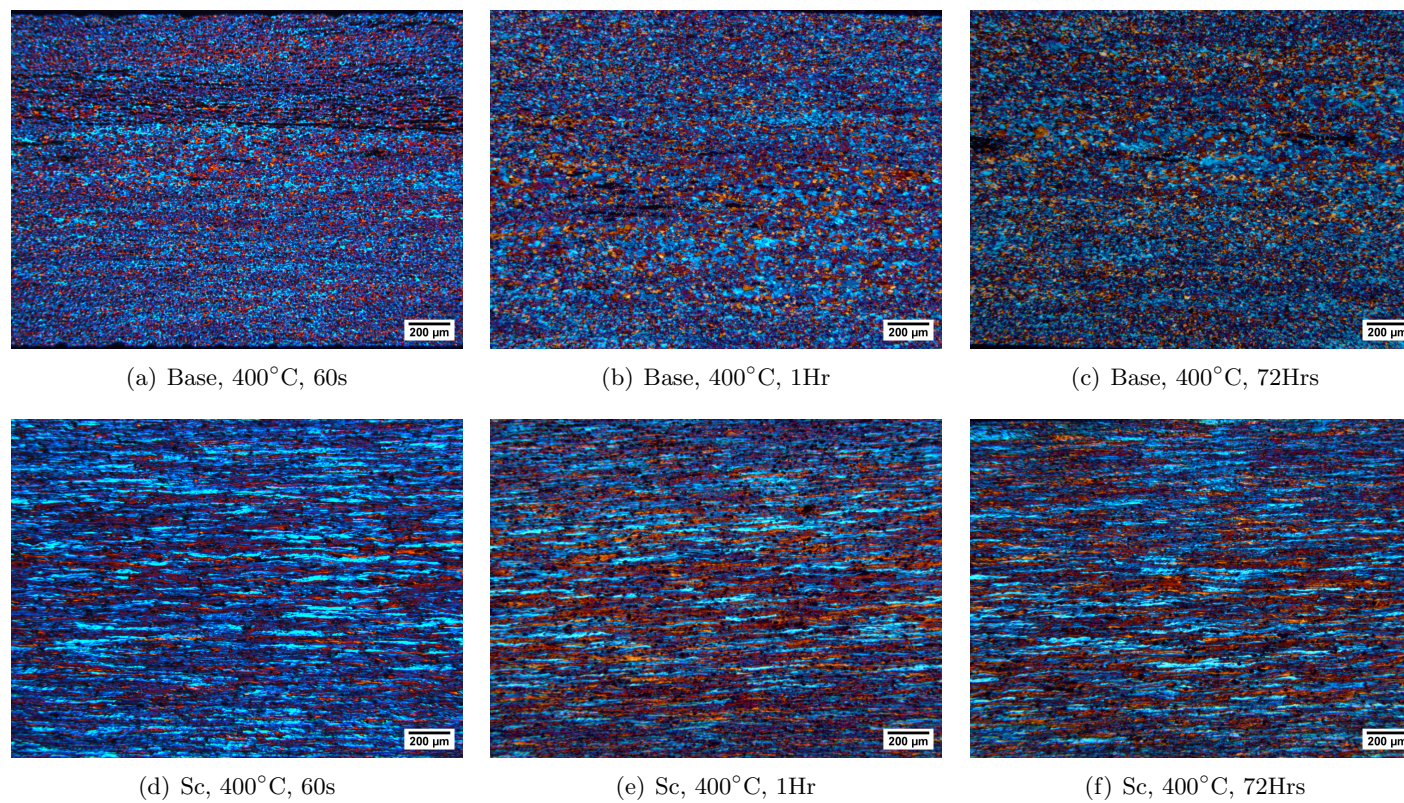


Figure 5.11: Through thickness optical micrographs of the base (top row) and Sc (bottom row) alloys. CR and aged at 400°C for 60seconds ((a) ,(d)), 1hour ((b),(e)) and 72 hours ((c), (f)).

5.3.2 Scanning Electron Microscopy

SEM/EDX analyses were performed on as cast samples in order to determine the elemental components of the intermetallic phases observed in optical metallography. Figures 5.12 and 5.13 show SEM results of the as cast microstructure of the two alloys. Images were obtained in Back Scatter Electron (BSE) mode. As mentioned in the previous section, mainly two types phases were observed in these alloys: firstly the intermetallic phases which appeared at grain boundaries ($5\mu m$ or less in size) observed in both alloys and secondly, the large ($20\mu m$ or greater) primary phases observed only in the Sc alloy. EDX analysis of the two alloys detected the phase present at grain boundaries to be $Al_x(Mn, Fe)_{1-x}$ containing particles in both alloys (Figures 5.12 and 5.14). In commercial Al alloys with low Si levels (in this case 0.05wt.%) these phases are most commonly $Al_6(Mn, Fe)$ phases [34]. In the Sc alloy, the large, primary phases observed were determined to be $Al_3(Sc_x, Zr_{1-x})$ phases. Of these phases, two types were observed. The first type, which contained equal levels of Sc and Zr, were star-shaped intermetallics (Figure 5.14). The second type, which contained higher levels of Zr than Sc, were mainly needle shaped particles (Figures 5.15). No SEM analysis was performed on the CR alloys.

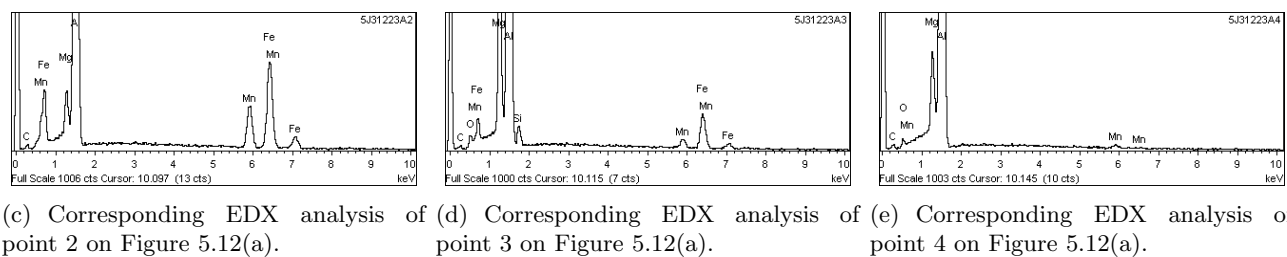
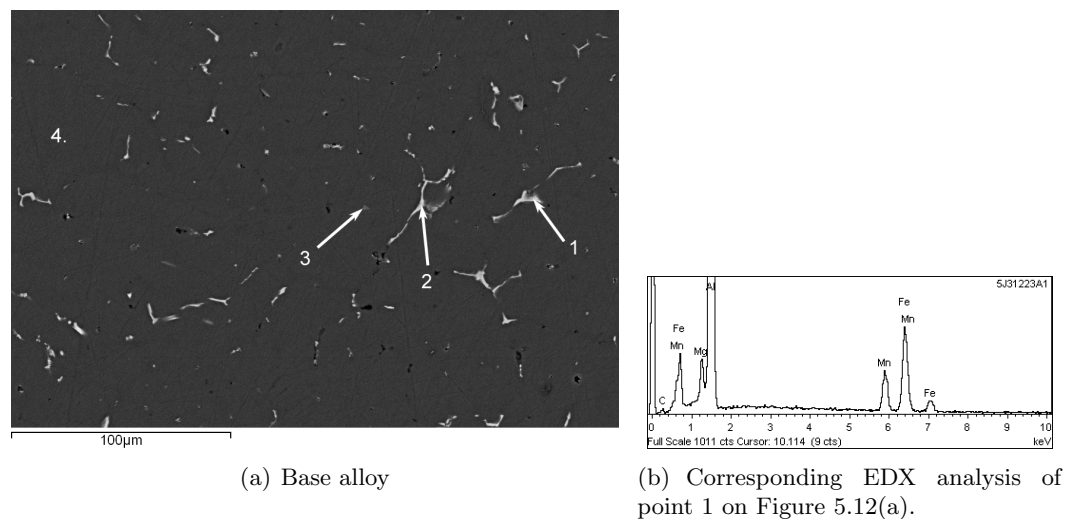
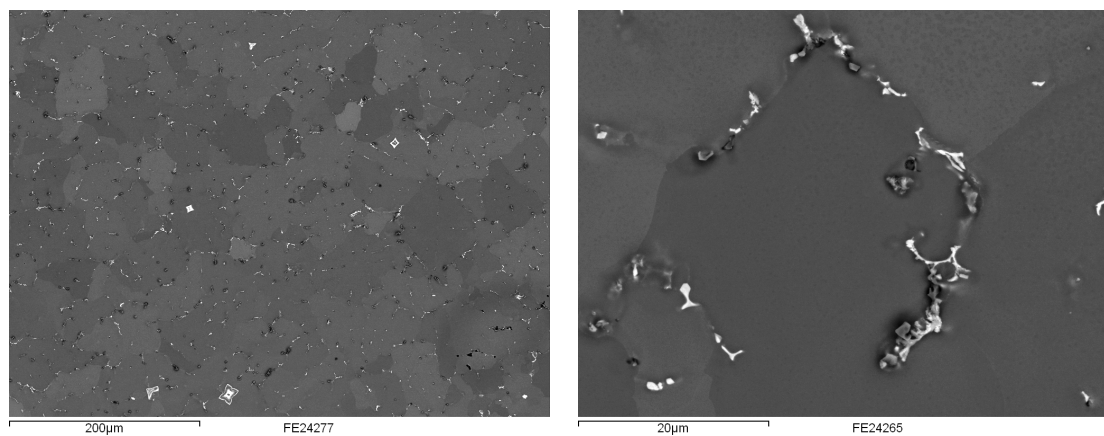
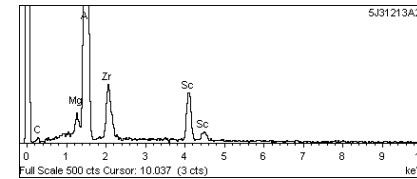
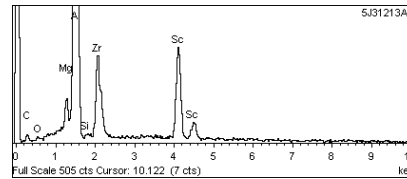
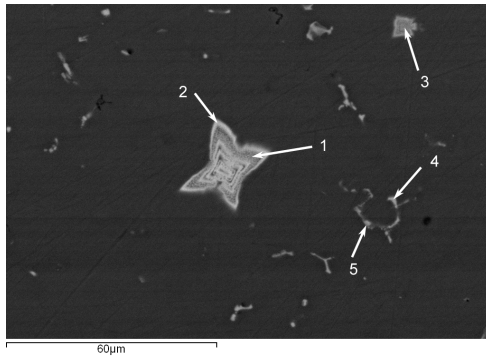


Figure 5.12: SEM Back Scatter Electron image of AC microstructure of the base alloy at approximately 1mm from cast surface, and corresponding EDX analysis of the intermetallics found in the structure. The EDX analysis suggest the intermetallics at grain boundaries are $Al(Fe, Mn)$ phases.

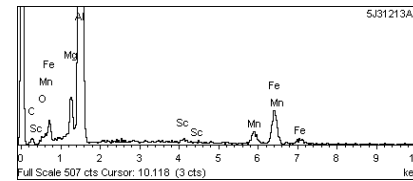
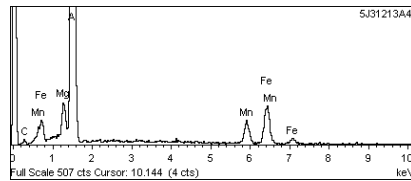
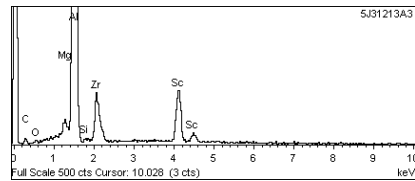


(a) Sc alloy, AC electropolished near surface plane. (b) Sc alloy, AC electropolished near surface plane

Figure 5.13: SEM Back Scatter Electron image of electropolished microstructure of the Sc alloy examined at approximately 1mm from cast surface. As can be seen through channeling contrast, the $Al(Mn, Fe)$ phases are concentrated on grain boundaries in the microstructure.



(a) Primary $Al_3(Sc_x, Zr_{1-x})$ phase, AC Sc alloy (b) Corresponding EDX analysis of point 1 on Figure 5.14(a). (c) Corresponding EDX analysis of point 2 on Figure 5.14(a).



(d) Corresponding EDX analysis of point 3 on Figure 5.14(a). (e) Corresponding EDX analysis of point 4 on Figure 5.14(a). (f) Corresponding EDX analysis of point 5 on Figure 5.14(a).

Figure 5.14: SEM Back Scatter Electron image of microstructure of the Sc alloy examined at approximately 1mm from cast surface and corresponding EDX analysis of the intermetallics found in the structure. The EDX analysis suggest the star-shaped intermetallics are $Al_3(Sc_x, Zr_{1-x})$ phases with equal Sc and Zr concentrations and the coarse phases at grain boundaries are $Al_x(Mn, Fe)_{1-x}$ phases which were also found in the base alloy.

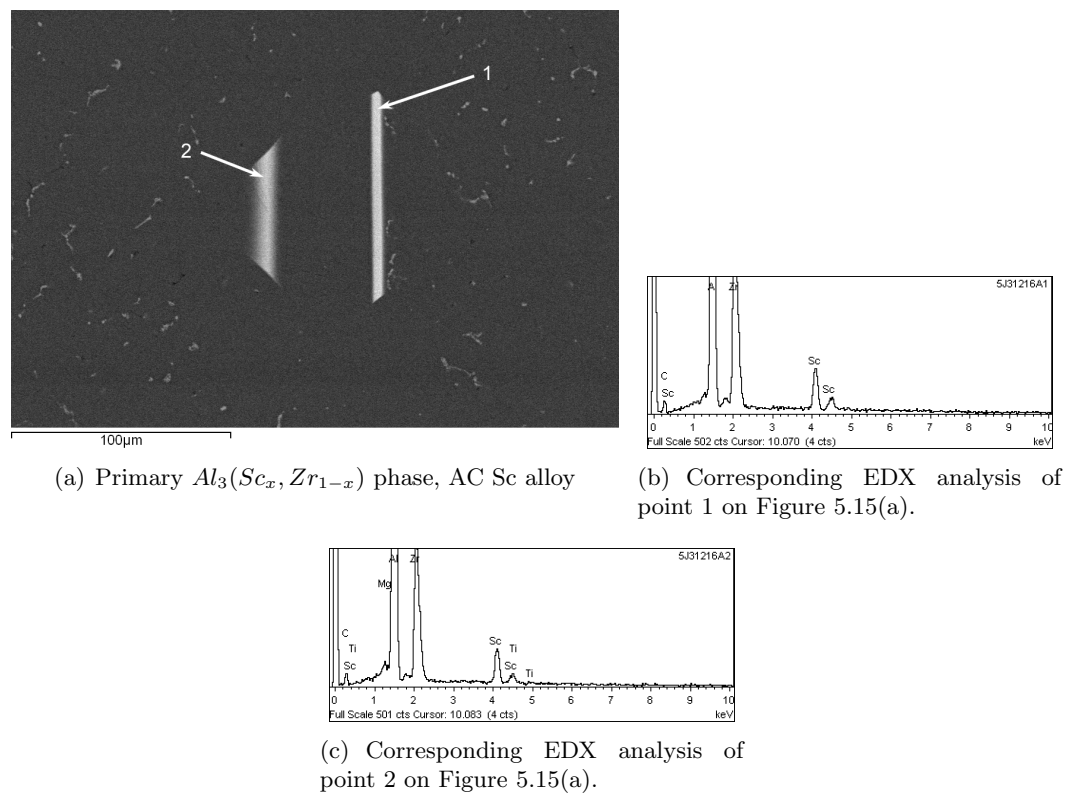


Figure 5.15: SEM image of microstructure of the Sc alloy examined at approximately 1mm from cast surface and corresponding EDX analysis of the intermetallics found in the structure. The EDX analysis suggest these needle-shaped intermetallics are $Al_3(Sc_x, Zr_{1-x})$ phases with higher concentrations of Zr than Sc.

5.3.3 Transmission Electron Microscopy

In order to examine the microstructure of the alloys in more detail and determine the presence of $Al_3(Sc, Zr)$ precipitates, TEM analysis was performed on AC, AC and aged, as-rolled, and CR and aged samples. Tables 2 and 3 summarize the conditions for which TEM analysis was performed for the base and Sc alloys respectively. The conditions for these samples were chosen based on the hardness data to examine the peak-aged and the over-aged conditions. The main aim of examining samples of the Sc alloy was to qualitatively determine if $Al_3(Sc, Zr)$ precipitates were present and if so, how they contribute to precipitation hardening and to thermal stability by pinning the deformed structure. Diffraction patterns were used for confirming presence of precipitates. In the case of Al_3Sc and Al_3Zr precipitates, superlattice spots were expected to be observed in the diffraction patterns since both these precipitates form $L1_2$ structures [2]. Examination of the base alloy samples on the other hand allowed for assessment of the degree of recovery and recrystallization in the alloy in the absence of Sc. The observations made of the AC and aged samples will be discussed first followed by the CR and aged conditions for both alloys. The TEM results presented in this section were obtained in collaboration with Dr. Kang at NGTC and are also discussed in detail in [54].

AC Microstructure - The AC microstructure of both alloys consisted mainly of coarse constituent particles located at grain boundaries as was shown in the previous section. No evidence of $Al_3(Sc_x, Zr_{1-x})$ precipitates or Al-Mn dispersoids were observed (Figures 5.16(a) and 5.16(b)).

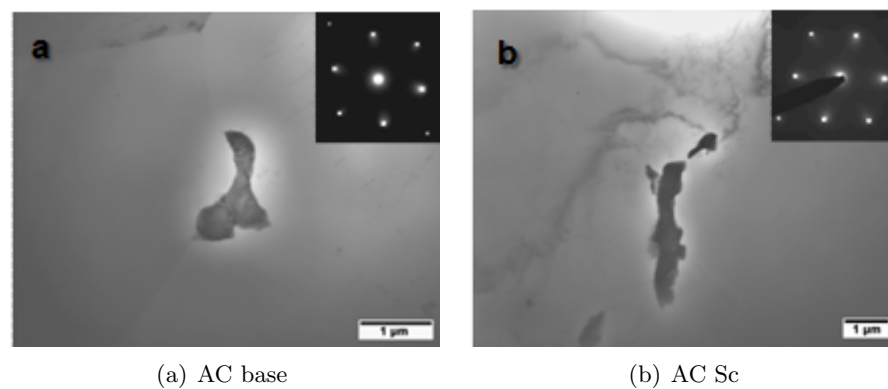


Figure 5.16: Bright field TEM images of AC microstructure of the (a) base and (b) Sc alloys showing the coarse $Al_x(Mn, Fe)_{1-x}$ constitutes observed in both alloys. The corresponding diffraction patterns of the matrix revealed no superlattice spots indicating no dispersoids had formed in the AC structure during solidification. [110] zone axis.

AC & Aged, Base Alloy - Two conditions were chosen for TEM analysis for the AC base samples: 300°C, 72 hours and 400°C, 30s. As shown in Figure 5.17(a), cubic Al_6Mn particles, approximately 100nm in size, had formed in the base alloy after aging for 72 hours at 300°C. Similar features were observed in the sample which was aged at 400°C for 30s (Figure 5.17(b)).

CR & Aged, Base Alloy - The same aging conditions chosen for the AC base alloy were chosen for the CR base alloy for TEM analysis (300°C, 72Hrs and 400°C, 30s). The first condition was chosen in order to examine the degree of recovery/recrystallization and second-phase precipitation in the base alloy. As shown in Figure 5.17(c), the sample aged at 300°C for 72Hrs shows an unrecrystallized but recovered microstructure. In the sample which was aged at 400°C for 30s however, complete recrystallization was observed along with fine Al_6Mn particles throughout the structure (Figure 5.17(d)). Figure 5.18 shows a higher magnification of the CR base alloy microstructure after aging at 300°C for 72Hrs (higher mag of Figure 5.17(c)). As can be seen in this image, fine Al_6Mn precipitates, approximately 100nm in size, have also formed throughout the structure.

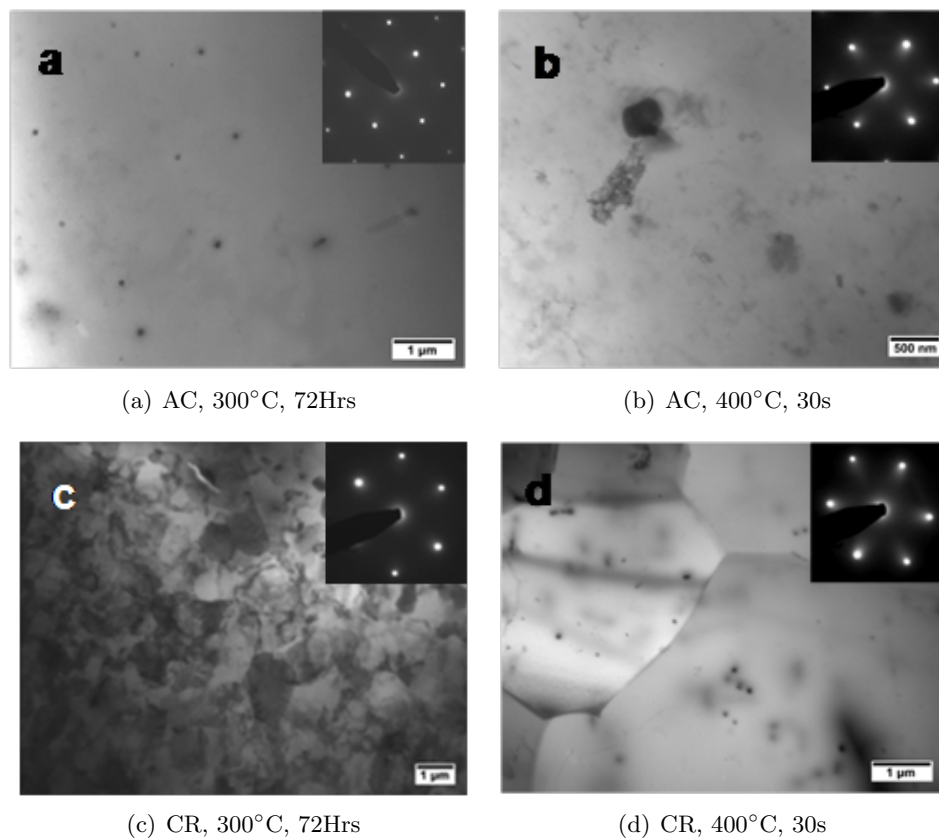


Figure 5.17: Bright field TEM images AC ((a) and (b)) and CR ((c) and (d)) of the base alloy at various aging conditions. The particles observed in these images are Al_6Mn phases precipitated during aging. A recovered microstructure is observed after aging at 300°C for 72Hrs while a completely recrystallized microstructure is seen after 30s of aging at 400°C 30s.

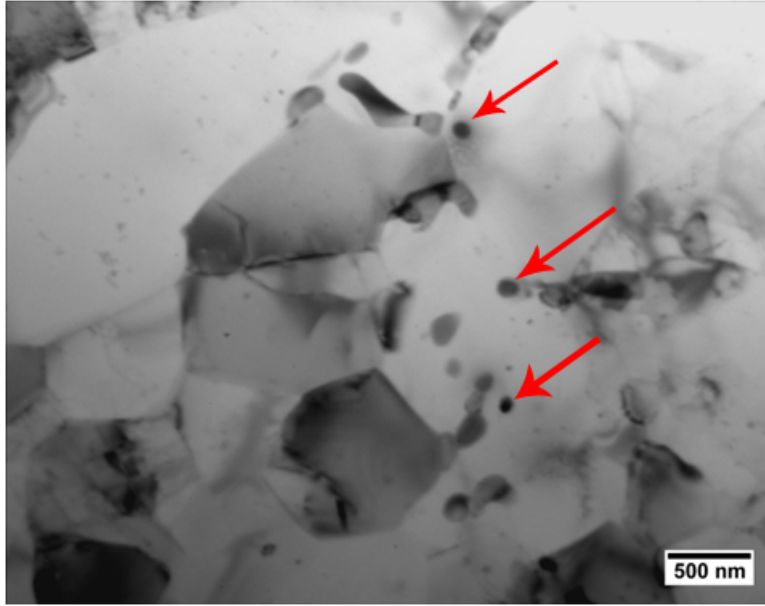


Figure 5.18: Higher magnification bright field TEM images CR microstructure of the base alloy after aging at 300°C for 72 hours. As can be seen in the image, fine Al_6Mn precipitates, approximately 100nm in size have formed during aging.

AC & Aged, Sc alloy - In the case of the AC Sc alloy, the following two aging conditions were chosen for TEM analysis: 300°C-24Hrs and 400°C-15 minutes, both representing the peak strength for these temperatures. TEM analysis of the sample aged at 300°C, showed coherent precipitates. The coherency of these precipitates is characterized by the Ashby-Brown contrast [55] observed in bright field TEM images (Figure 5.19(a)). Typically, the size of the precipitates is about half the size of the strain contrast. In this case, this contrast suggests that the size of the precipitates is approximately 10nm or less. The diffraction pattern shown in Figure 5.19(a) is consistent with those observed for Al_3Sc and/or $Al_3(Sc_x, Zr_{1-x})$ particles [56]. The sample

aged at 400°C for 15 minutes, also consisted of fine precipitates uniformly distributed throughout the sample (Figure 5.19(b)). This is also confirmed by the much higher brightness of the superlattice spots observed in this sample relative to the sample aged at 300°C. The distribution of these fine precipitates was homogeneous throughout both samples.

CR & Aged - Sc alloy CR Sc samples were aged at 300°C-4 hours and 400°C-1 minute for TEM analysis. As shown in Figure 5.19(c), fine coherent precipitates were also observed throughout the grains in the CR sample aged at 300°C as well as a high dislocation density. Figure 5.19(d), shows the microstructure of the sample aged at 400°C for 1 minute. Superlattice spots were also observed in this sample confirming that the particles observed are of the $Al_3(Sc_x, Zr_{1-x})$ phase. No sign of recrystallization was observed in any of the CR Sc samples (Figure 5.19).

As was seen in the TEM images shown in Figure 5.19, the $Al_3Sc/Al_3(Sc_x, Zr_{1-x})$ precipitates were smaller than 10nm for every condition which meant that examination of these precipitates was difficult. Therefore, samples aged at 400°C for 72 hours were also prepared in order to allow coarsening of the precipitates. Figures 5.20 and 5.21 show the TEM images for these samples in the AC and CR conditions respectively. As can be seen in these figures, the precipitates have retained their coherency even after 72 hours of aging at 400°C and, in the CR case, the structure has remained uncrystallized.

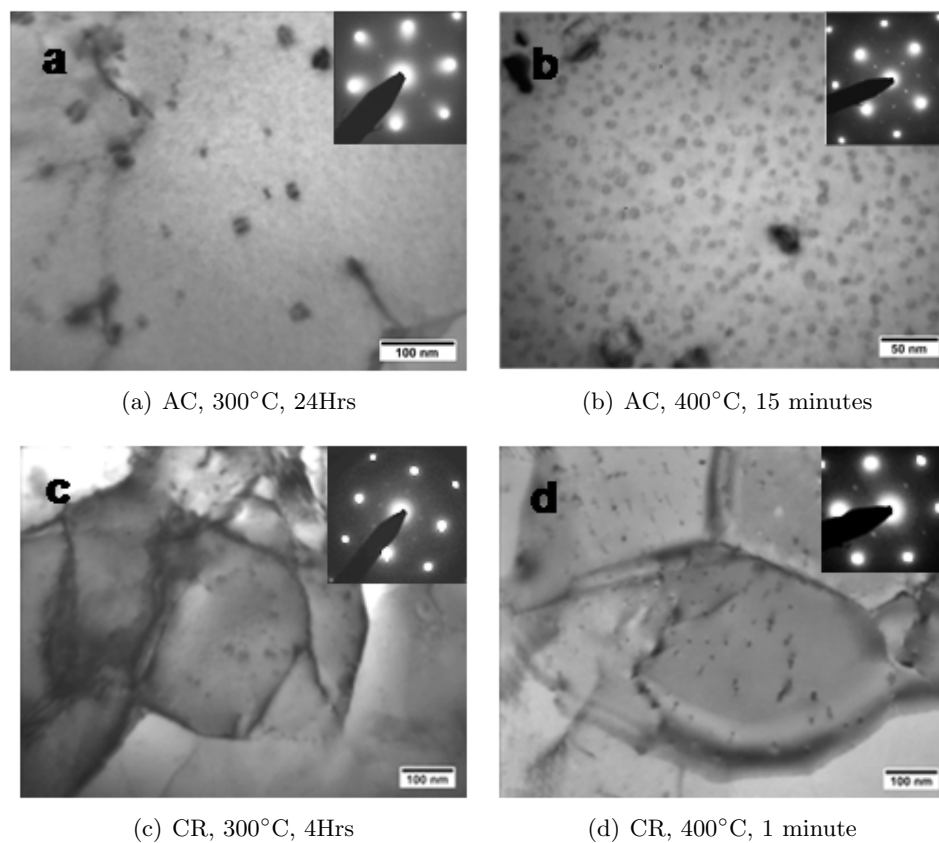


Figure 5.19: Bright field TEM images AC ((a) and (b)) and CR ((c) and (d)) of the Sc alloy at various aging conditions. The particles observed in these images are $Al_3(Sc_x, Zr_{1-x})$ phases precipitated during aging. A recovered microstructure is observed after aging at 300°C for 4Hrs as well as 400°C, 1 minute. Neither of the CR samples showed any sign of recrystallization.

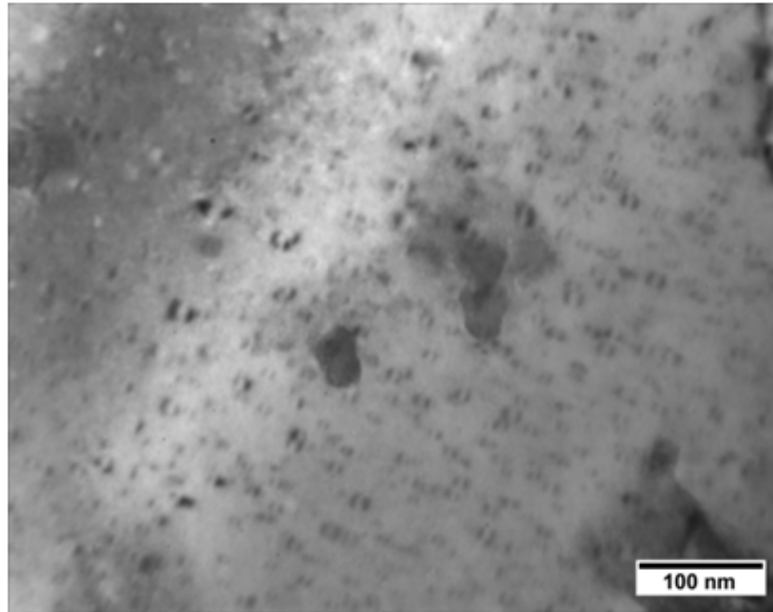


Figure 5.20: Bright field TEM image of the AC Sc alloy aged at 400°C for 72 hours. At this condition, the $Al_3Sc/Al_3(Sc_x, Zr_{1-x})$ precipitates have grown in size. However, as can be seen by the Ashby-Brown contrast, the precipitates have remained coherent even after 72 hours of aging.

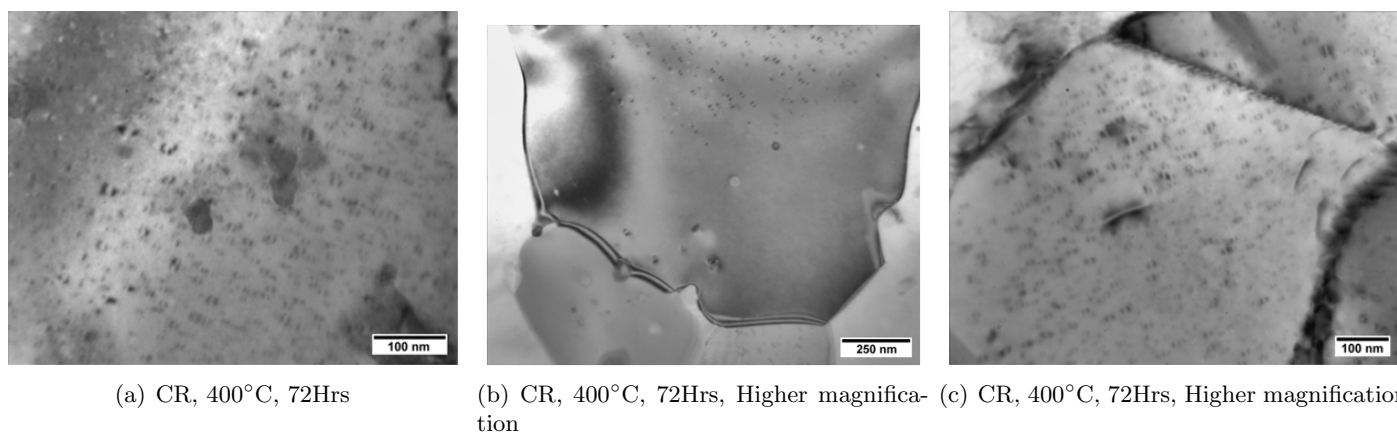


Figure 5.21: Bright field TEM image of the CR Sc alloy aged at 400°C for 72 hours. At this condition, the $Al_3Sc/Al_3(Sc_x, Zr_{1-x})$ precipitates have grown in size. However, as can be seen by the Ashby-Brown contrast, the precipitates have remained coherent even after 72 hours of aging and the structure has remained completely uncrystallized.

Chapter 6

Discussion

In this chapter the results presented in Chapter 5 are discussed. First, a correlation of the tensile strength and the hardness of the Sc alloy is presented. This correlation was used to estimate the tensile strength of the Sc alloy at various aging times. Next, the relative change in hardness and resistivity values are analyzed along with the corresponding microstructure. Then, a combination of these two correlations is used to estimate the yield strength increment due to precipitation hardening and the critical radius at which the shearable to non-shearable transition of the precipitates occurs. Finally, a summary of the results and discussion is presented.

6.1 Tensile Properties and Correlation of Hardness and Tensile Tests

As was shown in Figure 5.5, the peak yield strength (YS) for the CR Sc alloy was 384MPa which was reached after aging at 300°C for 4 hours. This YS value is comparable to the strengths reported in literature. Royset et al.

provided a summary of reported YS values of several investigations in [1]. Among these, a value of 368MPa was reported for an Al-5.3%Mg-0.3%Sc after a combination of cold-rolling and annealing at 343°C and aging at 288°C for 8 hours. The highest value was that of Al-6%Mg-0.5%Sc alloy at 433MPa. However, the higher Mg content of these alloys would be a significant contributing factor to these yield strengths. Fuller et al. performed a comparison of an AA5754 with that of a modified AA5754 with 0.23%Sc and 0.22%Zr additions. In this study, the YS of the conventional (O-temper) and modified AA5754 (as-rolled) alloys were reported to be 280 and 260MPa respectively [40]. Upon aging, the YS of the modified alloy decreased suggesting further annealing most likely only resulted in coarsening of the precipitates. Parker et al. reported a YS of 400MPa for a Al-4%Mg-1%Sc alloy aged at 290°C for 1 hour. However in this case a 300K/s cooling rate was used during casting [44]. Similarly, Sawtell et al. reported ≈ 470 MPa for a Al-4%Mg-0.56%Sc alloy which was semi-continuously cast and warm rolled at 288°C and then cold-rolled [43]. As can be seen from the above values, therefore, the YS of the Sc alloy in the present study is comparable with those of conventionally cast alloys as well as those cast with higher cooling rates which may be more relevant to TBC.

It is also interesting to note the elongation of the Sc alloy during various aging steps. As shown in Figure 5.3, the YS and the elongation of the Sc alloy samples both actually increase after aging and the as-rolled condition actually exhibits the lowest elongation ($\approx 4\%$ at fracture). After aging at 300°C for 4 hours the yield strength and the elongation of the alloy increased by approximately 30MPa and 5%, respectively. Typically, as a deformed mate-

rial is heat treated, strength decreases and elongation at break increases. In this case, however, the softening effect of recovery is offset by the precipitation hardening added due to Al_3Sc and/or $Al_3(Sc_x, Zr_{1-x})$ precipitates. Therefore an increase in yield strength is observed without a loss in ductility. As mentioned in the previous chapter, tensile tests were performed on the Sc alloy only at under-aged, peak-aged and over-aged conditions due to the limited amount of material available. Since alloy design specifications typically use yield/tensile strength values, a correlation was determined between the hardness and the yield/tensile strength of the Sc alloy. Using this correlation, the strength of the alloy was then calculated at all other aging times for which tensile properties were not measured.

It has been shown in the past that the tensile strength of Al alloys can be correlated with hardness by: $\sigma \approx H/3$ [57]. Therefore by plotting the yield and tensile strength values against the corresponding hardness values, a linear correlation between the yield/tensile strength and hardness of the alloy can be determined. These are shown in Figures 6.1 and 6.2 for the yield and tensile strengths, respectively. It should be noted that for this correlation, the hardness values were converted from VHN (kg/mm^2) to MPa ($1MPa = 9.8kg/mm^2$). Using these relationships, then the yield and tensile strengths of the alloy for all other other aging conditions can be estimated as shown in Figures 6.3 and 6.4.

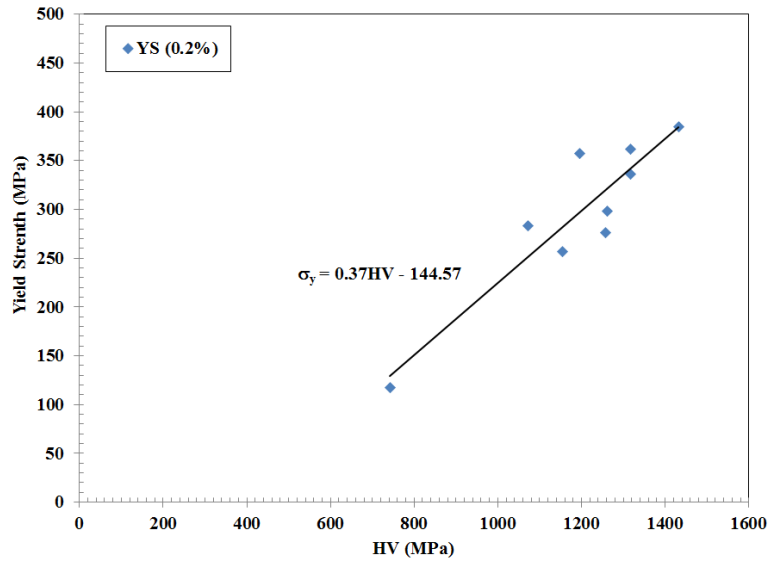


Figure 6.1: The correlation of the yield strength and corresponding hardness value for the Sc alloy. $R^2 = 0.84$.

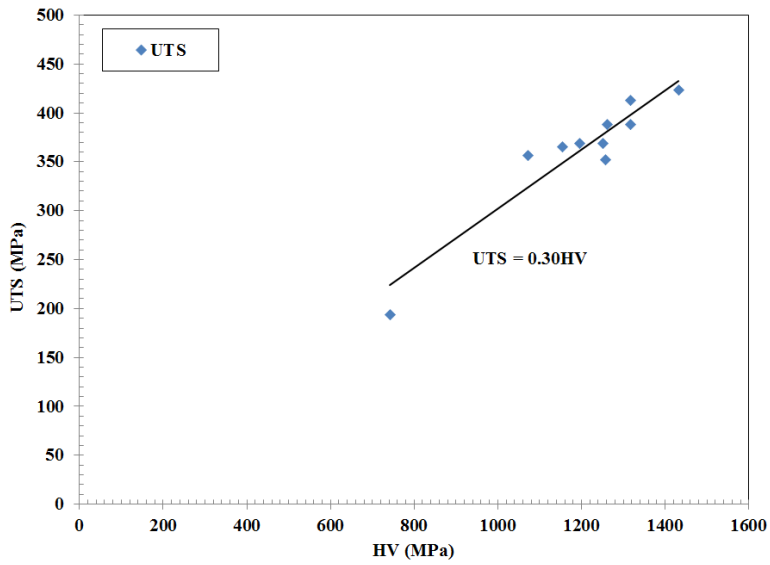


Figure 6.2: The correlation of the ultimate tensile strength and corresponding hardness value for the Sc alloy. $R^2 = 0.90$.

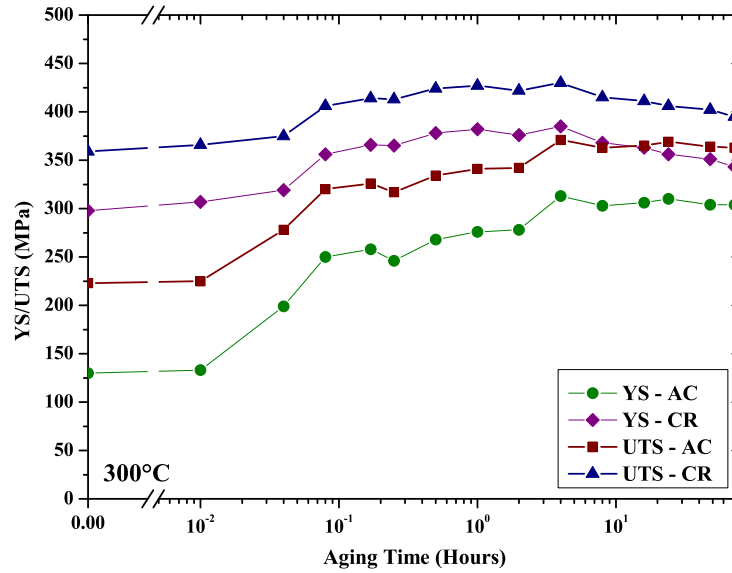


Figure 6.3: The estimated tensile and yield strengths of the Sc alloy for various aging times at 300°C. These estimations are obtained from a correlation of experimental tensile/yield strength and hardness values as shown in Figures 6.1 and 6.2.

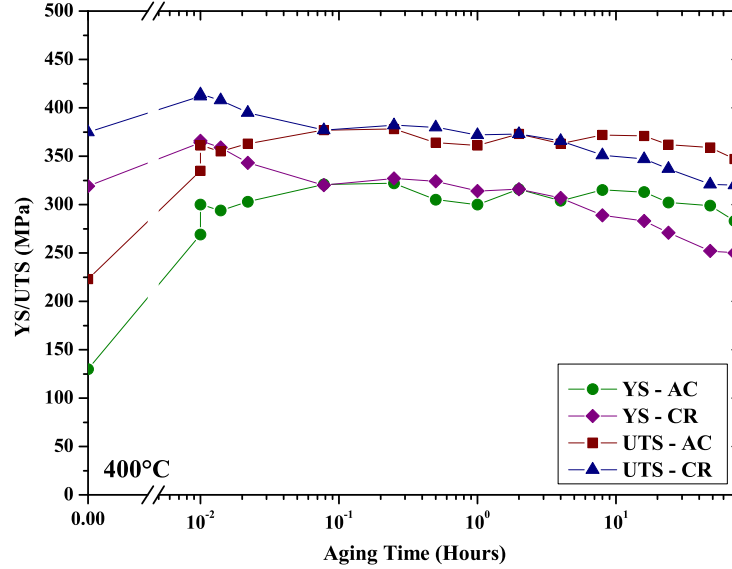


Figure 6.4: The estimated tensile and yield strengths of the Sc alloy for various aging times at 400°C. These estimations are obtained from a correlation of experimental tensile/yield strength and hardness values as shown in Figures 6.1 and 6.2.

6.2 Correlation of Hardness and Resistivity Results

As mentioned in Chapter 2, Twin Belt Casting (TBC) utilizes substantially higher cooling rates ($\approx 100\text{K/s}$) relative to conventional DC casting (1 - 10K/s). The high solidification rate of the TBC slab then results in a supersaturated solid solution in the as-cast structure. Therefore, the need for homogenization prior to cold-rolling is removed and consequently the alloy can be directly cold-rolled after casting. In the present case, the main alloying additions in the base alloy were Mn and Zr and Mn, Zr and Sc in the Sc

alloy. As mentioned in the previous chapter, SEM analysis of the AC microstructure of both alloys showed coarse $Al_x(Mn, Fe)_{1-x}$ constituents and in addition to these constituents, primary $Al_3(Sc_x, Zr_{1-x})$ phases were also observed in the Sc alloy. However, TEM examination of both alloys showed no sign of $Al_3(Sc_x, Zr_{1-x})$ precipitates (or superlattice spots), or Al_6Mn dispersoids, which indicated that other than the large constituent and primary phases, the remaining concentration of these alloying additions was in solid solution in the AC metal 5.16. It was expected therefore, that the $Al_3(Sc, Zr)$ and Al_6Mn precipitates could form during aging at intermediate temperatures ($200^\circ C < T < 400^\circ C$). As was discussed in the previous chapter, the effect of these precipitation reactions were monitored in two ways: hardness tests, and electrical resistivity measurements. Electrical resistivity measurements have been used in the past in order to evaluate the solid solution content in an alloy which can then indicate the degree of precipitation[29, 51, 58].

In order to examine the effect of precipitation in the base and Sc alloys, the change in hardness (ΔHV) and the change in resistivity ($\Delta\rho$) were determined (Figures 6.6(a) and 6.6(b)). This analysis was only conducted for results obtained from aging at 300 and 400°C since both alloys showed a much stronger response at these temperatures relative to aging at 200°C. ΔHV and $\Delta\rho$ were calculated according to equations 6.1 and 6.2, respectively:

$$\Delta HV = HV_{aged} - HV_0 \quad (6.1)$$

$$\Delta\rho = \rho_{aged} - \rho_0 \quad (6.2)$$

where HV_0 and ρ_0 are the hardness and resistivity of the alloys at zero aging time, respectively. Therefore for each aging step, the net change in hardness or resistivity relative to the initial AC or as-rolled measurement was calculated for each sample for the relevant condition. The change in hardness can be due to two main factors: precipitation, which increases the strength up to the peak-aged condition, and recovery or recrystallization, which lower the strength. There are several factors that contribute to changes in resistivity as shown in equation 6.3:

$$\rho_{Total} = \rho_{pure} + \rho_T + \sum_i \rho_i C_i + \rho_{\perp} + \rho_{ppt} + \rho_v \quad (6.3)$$

where, ρ_{pure} is the resistivity of pure aluminum, ρ_T is the resistivity contribution due to phonon scattering which is dependent on temperature, ρ_i and C_i are the resistivity coefficient and concentration of the solute in solid solution respectively, ρ_{\perp} is the additional scattering due to dislocations, ρ_{ppt} is the resistivity addition due to precipitates, and finally ρ_v is the scattering due to vacancies [58]. In this case the electrical resistivity measurements were taken at room temperature for all the aging steps and samples. This reduces any inconsistency in the results which may be due to temperature variations. Similarly, ρ_v is a very small contribution to the overall resistivity and can therefore be ignored [58]. The contribution of precipitates to resistivity has been shown to be most apparent during the initial stages of nucleation where precipitates are particularly fine and closely spaced together. The larger the spacing of the precipitates, the smaller this effect becomes. Previous studies on AA6111 have shown that the resistivity contribution of precipitates

is relevant only when the inter-particle spacing is less than 25nm [59]. As TEM observations presented in the previous chapter showed, the spacing of the Al_6Mn precipitates formed after aging, was larger than 100nm in both alloys. Since, the spacing of the Al_3Sc precipitates was observed to be approximately 25nm or larger in samples aged at 400°C 5.19, it is assumed that their contribution is substantially smaller than the effect of Sc in solid solution. Similar reasoning is applied to the resistivity contribution due to dislocations. Increasing the dislocation density has been shown to increase the resistivity of the alloy [51, 59]. A comparison of the resistivity measurements of the AC and AR alloys prior to aging however, indicates that this effect is also negligible compared to that of the solute elements as shown in Figure 5.7. Assuming a dislocation density of $\rho = 10^{15}m/m^3$ in the CR alloys, and given $2 \times 10^{-16}n\Omega m^3$ as the resistivity coefficient of dislocations, the resistivity contribution of dislocations amounts to approximately $0.2n\Omega \cdot m$ which is in agreement with the measurements shown in Figure 5.7. It is therefore reasonable to assume that the total resistivity of the alloy is primarily determined by the sum of the contributions of the solute elements and pure aluminum (which includes phonon scattering):

$$\rho_{Total} \approx \rho_{Al} + \sum_i \rho_i C_i \quad (6.4)$$

As an initial check on the applicability of equation 6.4, the resistivity of the alloys in this study can also be calculated using the resistivity coefficient and the corresponding concentration of each alloying addition as shown in Tables 6.1 and 6.2. This calculation yields 69.4 and $77.6n\Omega \cdot m$ for the

base and Sc alloys, respectively, which compares to 66.4 and $72.5 \pm 0.2 n\Omega \cdot m$ measured experimentally. Furthermore, as shown in Figure 5.7, the initial AC resistivity of the Sc alloy is $5.8 n\Omega \cdot m$ higher than that of the base alloy, which compares with an estimated value of $7.8 n\Omega \cdot m$ if all the Sc were in solid solution. This is a reasonable agreement, since as was observed in the SEM analysis of the AC structures of both alloys, coarse $Al(Mn, Fe)$ constituents were observed suggesting that not all of the Mn and Fe were in solid solution in the AC structure (see Figure 5.12). Furthermore, EDX analysis of the AC matrix revealed no Fe while small amounts of Mn were observed (Figure 5.12(a)). Therefore, since the solubility of iron in Al is also very low [60], it can be reasonably assumed that no Fe was retained in solid solution during casting. Removing the Fe contribution to the overall alloy resistivity yields 65.5 and $74.1 n\Omega \cdot m$ for the base and Sc alloys respectively which are closer to the measured values. In addition to the $Al(Mn, Fe)$ constituents, however, primary $Al(Sc, Zr)$ phases were also observed in the Sc alloy, illustrating that not all the Sc and Zr were in solid solution in this alloy either (Figure 5.14). It should also be noted that, there is some uncertainty in the resistivity coefficient values, although this is not specified in the reference [61]. The error associated with each resistivity measurement is $\pm 0.3 n\Omega \cdot m$.

AC Base Alloy - An examination of the annealing response of the base alloy in Figure 6.6(a) shows that there is a drop in resistivity of approximately 2 and $11 n\Omega \cdot m$ at 300 and 400°C respectively while only a small change in hardness is observed. The decline in resistivity in this case can be mainly

attributed to the precipitation of Al_6Mn particles. The precipitation of the Mn-containing particles was also confirmed through TEM analysis as shown in Figure 5.17. According to Table 6.1 [61], the resistivity coefficient of Mn in solid solution is $29.6n\Omega m/wt\%$. This coefficient is significantly higher than those of the other alloying additions present in the base alloy. Mn is also at a higher level than the other alloying additions after Mg, and has higher diffusivity at 400°C relative to 300°C resulting in more rapid precipitation kinetics. Another possible contributing factor would be precipitation of Zr in form of Al_3Zr particles. At 400°C the diffusivity of Zr is approximately thirty times slower than that of Mn ($D_{Zr,400^\circ\text{C}} \approx 1.2 \times 10^{-20} m^2/s$, $D_{Mn,400^\circ\text{C}} \approx 4.0 \times 10^{-19}$). Therefore it is likely that Zr is also precipitating out of solid solution during aging at 400°C . However, further TEM analysis is required in order to confirm the presence of Al_3Zr precipitates. However at 300°C , the precipitation of Mn is approximately 100 times faster than that of Zr, therefore it is unlikely that significant amounts of Zr would precipitate out of solid solution at this temperature. Therefore, it is reasonable to assume that the $11n\Omega \cdot m$ drop in resistivity in the base AC alloy is due to the combined effect of Mn and Zr precipitation. Referring to the Al-Mn phase diagram (Figure 6.5), it can be seen that at 400°C , the solubility of Mn is approximately 0.05wt% indicating that the precipitation of Mn has not yet reached equilibrium after 72 hours. Similarly, at 300°C , the solubility of Mn is almost zero, however only a drop of $2n\Omega \cdot m$ was observed after 72 hours of aging. Solubility of 0.008 and 0.05wt%Mn at 300 and 400°C , would correspond to equilibrium resistivity values of 16.3 and $15.1n\Omega \cdot m$, respectively. The long time required for the precipitation of Mn can be at-

tributed to the low diffusivity of Mn in Al ($\approx 5 \times 10^{-22}$ and $\approx 4 \times 10^{-19} m^2/s$ at 300 and 400°C respectively [14]). Similarly, the solubility of Zr is also approximately zero at 300 and 400°C (0.28wt% at 660°C [60]). Consequently, at $17.7 n\Omega \cdot m / wt\%$ and 0.2wt% Zr, the equilibrium resistivity value for Zr would be approximately $4 n\Omega \cdot m$. The sum of the contributions of Mn and Zr would therefore correspond to a change of 20.4 and $19.2 n\Omega \cdot m$ at 300 and 400°C, respectively, as shown in Figure 6.6(a). Examining the hardness results, it can be observed that there is almost no change for the AC base alloy indicating that the precipitation of Mn does not produce significant precipitation hardening.

Table 6.1: Resistivity coefficients (coeff) and resistivity contribution of each element (ρ_i) in the base alloy. ρ_i is determined by multiplying the wt% of each element by the corresponding coeff. [61].

Base Alloy	Mg	Mn	Sc	Zr	Fe	Ti	Si	V	Ni	Zn	Cu	Cr	Al	
Coeff ($n\Omega \cdot m/\text{wt}\%$)	5.4	29.6	20.1	17.7	23.2	28.97	6.25	36.9	8.2	0.9	3.4	40.3		
$\rho_i(n\Omega \cdot m)$	17.0	16.6	0.0	4.1	3.9	1.4	0.1	0.4	0.0	0.0	0.0	0.0	26.6	
Measured Resistivity ($n\Omega \cdot m$)												68	Sum	69.4

Table 6.2: Resistivity coefficients (coeff) and resistivity contribution of each element (ρ_i) in the Sc alloy. ρ_i is determined by multiplying the wt% of each element by the corresponding coeff. [61].

Sc Alloy	Mg	Mn	Sc	Zr	Fe	Ti	Si	V	Ni	Zn	Cu	Cr	Al	
Coeff ($n\Omega \cdot m/\text{wt}\%$)	5.4	29.6	20.1	17.7	23.2	28.97	6.25	36.9	8.2	0.9	3.4	40.3		
$\rho_i(n\Omega \cdot m)$	16.5	16.6	7.8	4.3	3.5	1.6	0.3	0.4	0.0	0.0	0.0	0.1	26.6	
Measured Resistivity ($n\Omega \cdot m$)												73	Sum	77.6

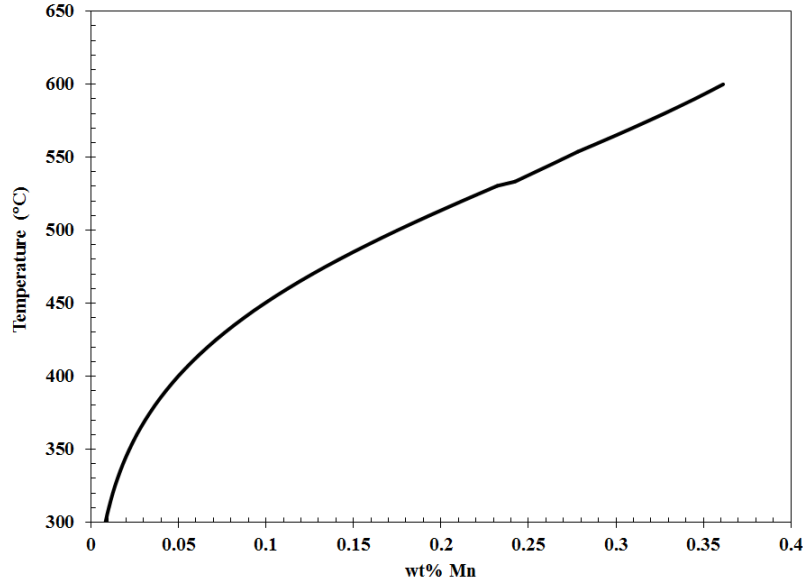
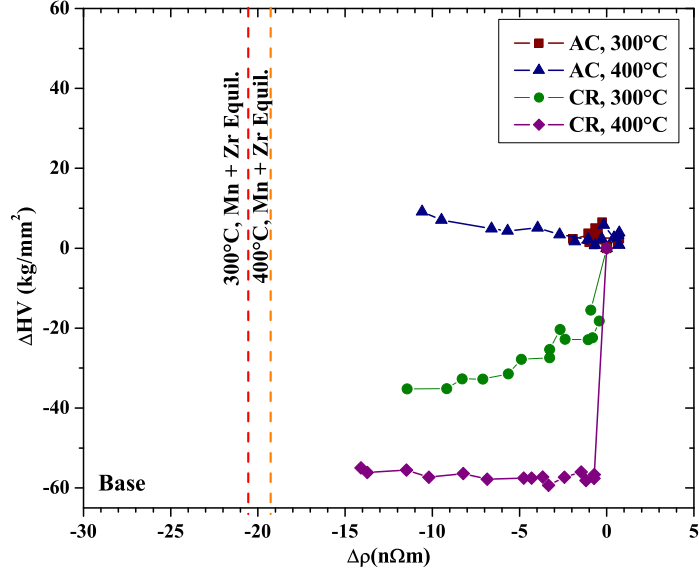


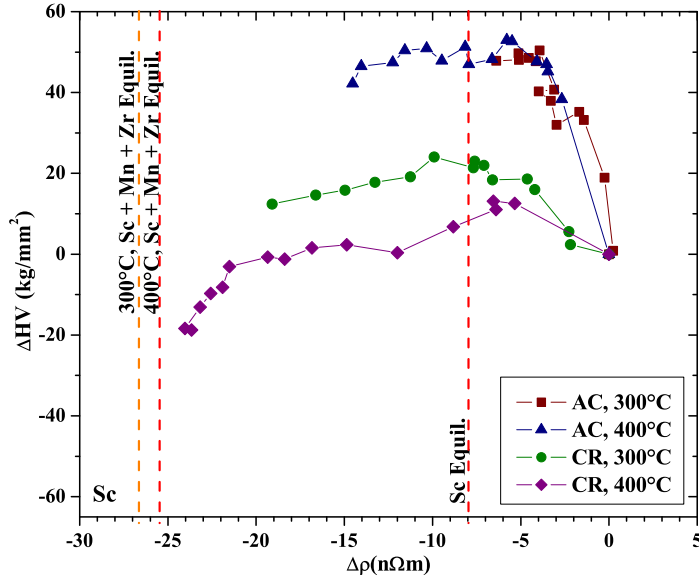
Figure 6.5: The Al rich corner of the Al-Mn phase diagram calculated for an Al-3%Mg-0.5%Mn-0.1%Fe-0.05%Si (base alloy) using ThermoCalc using TTA16 database.

AC Sc Alloy - In the Sc alloy (Figure 6.6(b)) an increase in hardness and a decrease in resistivity are observed at both 300 and 400°C in the AC material. Similar to the base alloy, a larger decrease in resistivity is observed at 400°C compared to 300°C (Figure 6.6(b)). However, in this case, the precipitation of Al_3Sc and/or $Al_3(Sc, Zr)$ enhances the hardness of the alloy. The variation in resistivity in this alloy, however, is a combined effect of Mn and Sc (and Zr) precipitation from solid solution. In the AC Sc alloy, a maximum reduction of $14.5n\Omega \cdot m$ takes place while only $11n\Omega \cdot m$ was observed in the AC base alloy during aging at 400°C. Referring to Figure 5.7(c), it can be seen that an initial rapid drop of $5.8n\Omega \cdot m$ is observed

in the AC Sc alloy by 15 minutes of aging. Over the same time period, the resistivity of the AC base alloy was observed to change very little. After 15 minutes of aging, the same level of decline in resistivity is observed in both alloys. Since, the reduction in resistivity for the base alloy is attributed to precipitation of Al_6Mn and Al_3Zr , it will be proposed that the same Mn and Zr precipitation reactions are occurring in the Sc alloy. Therefore the decline in resistivity in the Sc alloy after 15 minutes can be attributed to a combination of Mn, Zr and Sc precipitation and the initial $5.8n\Omega \cdot m$ decline can be solely due to Sc precipitation. This delay in the precipitation of Mn and Zr in the AC structure can be attributed to the slow diffusivity of Mn and Zr in Al ($D_{Mn} \approx 4 \times 10^{-19} m^2/s$, $D_{Zr} \approx 1.2 \times 10^{-20} m^2/s$ at $400^\circ C$ [14]). The diffusivity of Sc however, although still very low, is faster than that of Mn in Al ($D_{Sc} \approx 2 \times 10^{-17} m^2/s$ [14]). Therefore it is not surprising that the Sc precipitation occurs earlier than Mn precipitation.



(a) Base Alloy



(b) Sc-containing alloy

Figure 6.6: The change in hardness vs the change in resistivity during aging at 300 and 400°C for (a) base alloy (b) Sc alloy for the AC (open symbols) and CR (filled symbols) conditions.

Base Alloy, 80% CR - The curve for the CR base alloy at 300°C shows an $11n\Omega \cdot m$ drop in resistivity while almost no change in resistivity occurs in the AC base alloy (Figure 6.6(a)). At 400°C, a drop of $11n\Omega \cdot m$ and $14n\Omega \cdot m$ occur for the AC and CR base alloys respectively. The higher decline in resistivity for the CR alloys suggests that the initial deformed structure has an influence on the precipitation of Mn. The presence of dislocations can enhance diffusivity through pipe diffusion and provide nucleation sites for Mn precipitation and thus a finer distribution of precipitates could develop in a highly deformed structure relative to an AC one [62, 63]. As was mentioned above, the solubility of Mn in Al is approximately 0.05wt% at 400°C (Figure 6.5), which corresponds to a resistivity contribution of $15.1n\Omega \cdot m$. Similarly, the resistivity contribution of Zr was determined using the resistivity coefficient to be $4n\Omega \cdot m$. This agrees well with the change in resistivity of the base alloy after 72 hours of aging. The decline in hardness in the CR base alloy is also more prominent at 400°C relative to 300°C. At 400°C a rapid drop of 55VHN is observed indicating complete recovery and recrystallization. This result was confirmed by OM and TEM examination of the sample aged at 400°C for 1 minute, which exhibited a completely recrystallized grain structure (Figures 5.11 and 5.17). At 300°C, however, a reduction of only 35VHN occurs. In this case, OM and TEM examination of samples aged at 300°C for 72 hours revealed an unrecrystallized but recovered structure (Figures 5.10 and 5.17). TEM examination of these samples also confirmed that Mn-containing particles had precipitated in both samples. This effect is a result of a competition between recrystallization and Mn precipitation in the CR base alloy. If significant Mn precipitation occurs prior to recrystallization,

the deformed structure is pinned by the Mn-containing particles, thereby inhibiting recrystallization, which is the case at 300°C. At 400°C, however, these particles form after recrystallization has occurred. This effect is also evident in Figures 5.1 and 5.7. At 300°C, the hardness of the CR alloy decreases at a higher rate up to 5 minutes of aging. After 5 minutes, a more steady decrease is observed (Figure 5.1(b)). Referring to the corresponding resistivity change (Figure 5.7(b)), the opposite trend is observed. Resistivity is steady prior to 5 minutes and shows a more rapid drop afterwards. These trends can be attributed to the formation of Al_6Mn particles. Since the diffusivity of Mn is very low even when including possible pipe diffusion, the precipitation reaction requires a longer time for the precipitates to reach a size and volume fraction that would have a significant effect on the recovery of the alloy. During the initial stages of aging, since Al_6Mn precipitates have not formed yet, the hardness of the alloy drops rapidly due to recovery. As aging progresses, Al_6Mn particles form and slow down the recovery process. The formation of these Al_6Mn particles also explains the more rapid drop in resistivity in the later stages of aging. A similar pattern is observed for the base alloy aged at 400°C. In this case, however, the decline in resistivity becomes more prominent after 1 hour of aging indicating the precipitation of Al_6Mn . At this temperature, the kinetics of recrystallization are faster and therefore the formation of these precipitates does not inhibit recovery or recrystallization as was observed in the results for 300°C.

Sc Alloy, 80% CR - The situation for the CR Sc alloy, is more complex. As shown in Figures 5.1(c) and 5.7(c), a rapid increase in hardness is observed

after just 1 minute of aging along with a corresponding rapid decline in resistivity. Here, concurrent softening (recovery) and precipitation of Sc and Mn is expected; with the precipitation kinetics being influenced by the dislocation network. Referring to Figure 6.6(b), a drop of $14n\Omega \cdot m$ can be seen for the base alloy while a reduction of $23n\Omega \cdot m$ is seen in the Sc alloy at 400°C . A comparable effect occurs during aging at 300°C . As shown in Figure 6.6(b), the equilibrium resistivity values for Sc, Mn and Zr added together ($-6.1 + -15.1 - 4.0 = -25.3n\Omega m$) result in approximately -26.5 and $-25.3n\Omega \cdot m$ for 300 and 400°C respectively. As can be seen from the figure, the precipitation reactions have not reached equilibrium.

6.3 Estimation of the Volume Fraction and Critical Radius

Thus far, the relationships between the changes observed in hardness, resistivity, and tensile strength have been discussed. It was shown that the change in resistivity in the base alloy during aging is attributed to the precipitation of Mn, the increase in hardness in the Sc alloy was due to precipitation of Al_3Sc and/or $Al_3(Sc_x, Zr_{1-x})$ particles, and finally that the change in resistivity in the Sc alloy was due to concurrent precipitation of Mn and Sc. The CR Sc alloy presented the most complex case where the effects of concurrent recovery and precipitation of Mn and Sc were linked in a complex manner. This effect is however simplified in case of the AC Sc alloy where dislocations are absent. Therefore, assuming that the precipitation of Mn and Sc are independent in a non-deformed matrix, the isolated effect of Sc precipitation can be calculated. This is a reasonable assumption

since Mn and Sc precipitation have been reported to be independent of each other in Al alloys [1, 14]. Consequently, it will be assumed that the Mn precipitation reaction occurs at the same rate in the Sc alloy as in the base alloy. In order to determine the effect of Sc independently, therefore, the hardness and resistivity of the base alloy can be subtracted from those of the Sc alloy at each aging step as described by the following equations:

$$\Delta HV' = HV_{Sc} - HV_{Base} \quad (6.5)$$

$$\Delta \rho' = \rho_{Sc} - \rho_{Base} \quad (6.6)$$

This is shown in Figures 6.7 and 6.8, where the net resistivity and hardness at 300 and 400°C, respectively, are plotted against aging time. As can be seen, the hardness of the alloy increases by approximately 54VHN and resistivity drops by $4.5n\Omega \cdot m$ after 4 hours at 300°C, and 56VHN and $5.5n\Omega \cdot m$ after 15 minutes at 400°C. As was shown in Figures 5.1(b) and 5.1(c), 4 hours and 15 minutes are the peak-aged condition for the Sc alloy at 300 and 400°C respectively. Figure 6.9 shows the same net hardness and resistivity results plotted against each other up to the peak aged conditions. As can be seen, a steady increase in hardness and a corresponding decrease in resistivity is observed which can be attributed to the precipitation of Sc.

As mentioned earlier, resistivity measurements can be used to indicate the degree of solute depletion from solid solution. Therefore, if the composition of the precipitate is known, resistivity can be used to also estimate the volume fraction of the precipitates assuming that solute depletes in atomic proportion to the composition of the precipitates. In this case, the net resis-

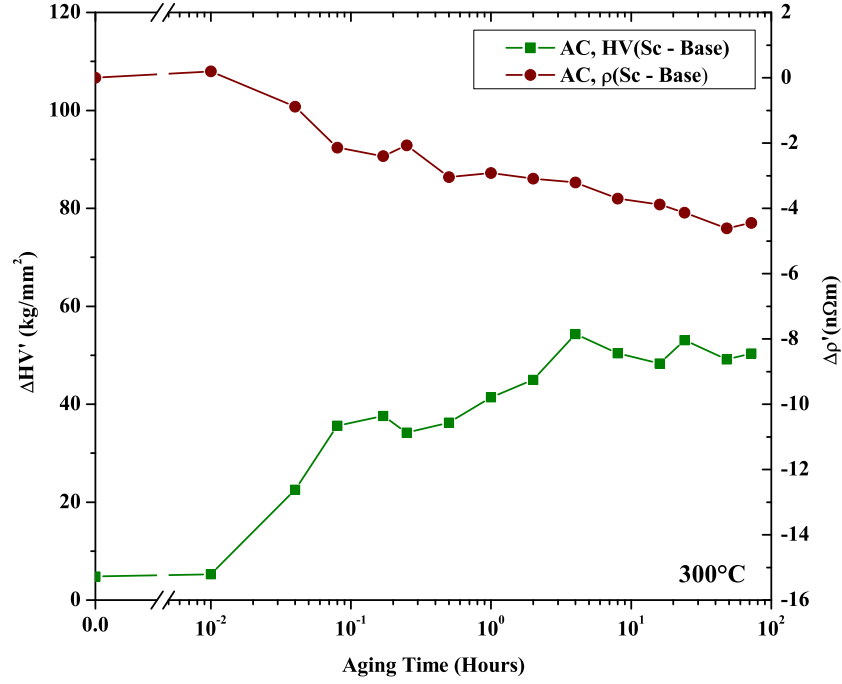


Figure 6.7: The difference between the hardness/resistivity of Sc alloy (HV_{Sc}/ρ_{Sc}) and the base alloy (HV_{Base}/ρ_{Base}) up to the peak-aged condition vs. aging time at 300°C in the AC condition. This result is the contribution of Sc precipitation to hardness and resistivity in the base alloy. Note: It has been assumed that the Mn and Sc precipitation reactions are independent.

tivity shown in Figure 6.9 can be used to estimate the depletion of Sc from solid solution and thereby the volume fraction of the Al_3Sc precipitates.

The net resistivity change shown in equation 6.6 is due to the precipitation of Sc out of solid solution. Therefore it can also be expressed as:

$$\Delta\rho' = \rho_{Sc}\Delta C_{Sc,SS} \quad (6.7)$$

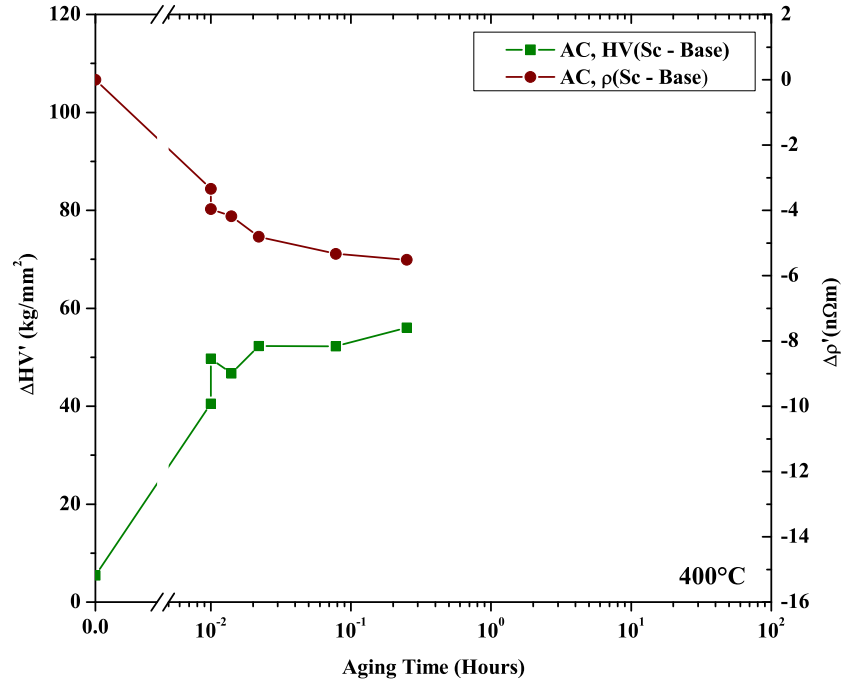


Figure 6.8: The difference between the hardness/resistivity of Sc alloy (HV_{Sc}/ρ_{Sc}) and the base alloy (HV_{Base}/ρ_{Base}) up to the peak-aged condition vs. aging time at 400°C in the AC condition. This result is the contribution of Sc precipitation to hardness and resistivity in the Sc alloy. Note: It has been assumed that the Mn and Sc precipitation reactions are independent.

where ρ_{Sc} is the specific resistivity of Sc ($n\Omega \cdot m/at\%$) and $\Delta C_{Sc,SS}$ is the change in atomic percent of Sc in solid solution. As mentioned above, the AC structure of the Sc alloy showed large primary intermetallics containing Sc and Zr which indicated that not all the Sc was in solid solution in the AC structure. However, $\Delta\rho'$ only takes into account the resistivity contribution of Sc in solid solution. Since the only significant compositional

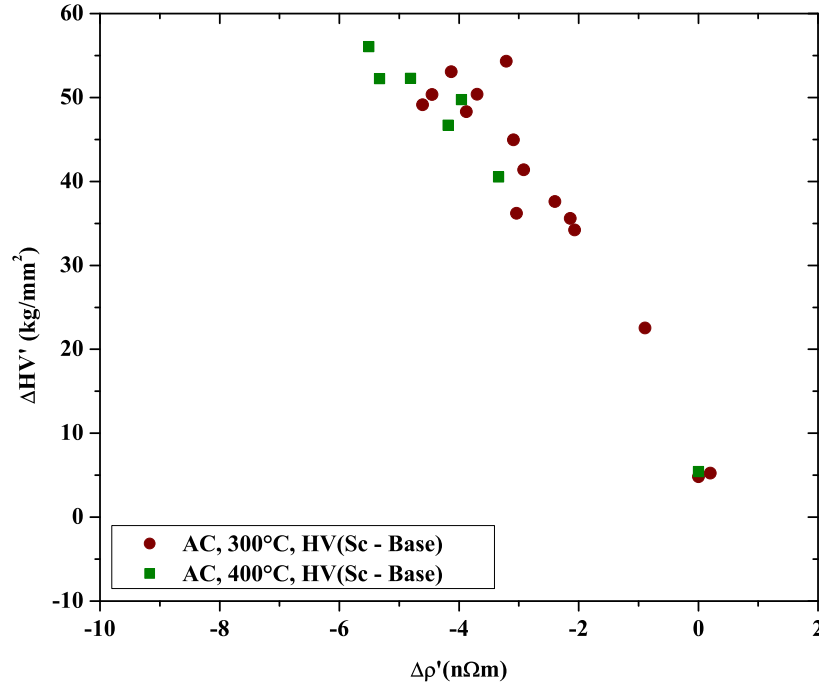


Figure 6.9: The difference between the hardness of Sc alloy and the base alloy up to the peak-aged condition at 300 and 400°C in the AC condition. The peak-aged condition occurs after 4 hours at 300°C and 15 minutes at 400°C. At each aging step, the hardness/resistivity of the base alloy is subtracted from that of the Sc alloy: $\Delta HV = HV(Sc - Base)$ and $\Delta\rho = \rho(Sc - Base)$. This result is the isolated effect of Sc in the Sc-containing alloy. Note: It has been assumed that the Mn and Sc precipitation reactions are independent.

difference between the two alloys is 0.23at%(0.387wt% Sc), by subtracting the resistivity of the base alloy from that of the Sc alloy (i.e. $\Delta\rho'$), the resistivity contribution of Sc is obtained. At zero aging time, $\Delta\rho' = 6.1n\Omega \cdot m$ which corresponds to 0.18at%Sc. The composition of Sc in the Sc alloy

was determined by ICP analysis to be 0.23at% (0.387wt%) indicating that approximately 20% of Sc was lost in the large primary intermetallics. As Al_3Sc precipitates form, the change in $\Delta\rho'$ would correspond to the change in the fraction of Sc in solid solution and respectively, the amount of Sc in the Al_3Sc precipitates. By mass balance, therefore, $\Delta C_{Sc,SS}$ can also be written as:

$$\Delta C_{Sc,SS} = \Delta C_{Sc,ppt} \quad (6.8)$$

where $\Delta C_{Sc,ppt}$ is the atomic fraction of Sc atoms in Al_3Sc precipitates. The atomic fraction of the Al in the precipitates is 3 times that of Sc ($C_{Al,ppt} = 3C_{Sc,ppt}$). Therefore, the volume fraction of Al_3Sc precipitates can be determined by:

$$\begin{aligned} f_{Al_3Sc} &= \frac{V_{molar}^{ppt} (mol_{Sc}^{ppt} + mol_{Al}^{ppt})}{V_{molar}^{matrix} \times mol_{Al}^{matrix}} \\ &= \frac{V_{molar}^{ppt}}{V_{molar}^{matrix}} (C_{Sc,ppt} + C_{Al,ppt}) \\ &= \frac{V_{molar}^{ppt}}{V_{molar}^{matrix}} (4C_{Sc,ppt}) \end{aligned} \quad (6.9)$$

where $V_{molar}^{ppt} = 1.04 \times 10^{-5} m^3/mol$ is the molar volume of Al_3Sc [11] and $V_{molar}^{matrix} = 1 \times 10^{-5} m^3/mol$ is the molar volume of Al [59]. Equation 6.9 can be solved for the fraction of Sc in Al_3Sc precipitates:

$$C_{Sc,ppt} = \frac{f_{Al_3Sc} V_{molar}^{matrix}}{4V_{molar}^{ppt}} \quad (6.10)$$

Substituting equation 6.10 into equation 6.7:

$$\Delta\rho' = \rho_{Sc} \left(\frac{f_{Al_3Sc} V_{molar}^{matrix}}{4V_{molar}^{ppt}} \right) \quad (6.11)$$

therefore:

$$f_{Al_3Sc} = \frac{4\Delta\rho' V_{molar}^{ppt}}{\rho_{Sc} V_{molar}^{matrix}} \quad (6.12)$$

Using equation 6.12, the volume fraction of Al_3Sc can be calculated.

As mentioned in chapter 2, the effect of precipitates on yield strength is mainly obtained through the interaction of precipitates with dislocations. As precipitates grow the force required by dislocation to pass the precipitates increases until the precipitates have reached a critical size, r_c . When the precipitate radius is smaller than r_c , the passing dislocation can shear the precipitate. Above r_c however, the precipitates are non-shearable, the force inserted by the dislocation on the precipitates reaches a maximum value and the dislocation forms a loop around the particle (Figure 6.10). This is referred to as Orowan mechanism.

If the volume fraction of the precipitates is known, r_c can also be estimated as follows. As mentioned in chapter 2, the effect of precipitates on yield strength can be modeled by [23]:

$$\sigma_{ppt} = \frac{MF}{bL} \quad (6.13)$$

where M is the Taylor Factor, F is the interaction force between a precipitate and a dislocation, b is the Burgers vector and L is the average effective spacing between the precipitates. Assuming that the force is proportional

to the radius of the Al_3Sc precipitates, and that the average radius of the precipitates is below the critical radius ($r \leq r_c$), F can be determined by:

$$F = 2T \frac{r}{r_c} \quad (6.14)$$

where,

$$T = \alpha G b^2 \quad (6.15)$$

, substituting equation 6.15 into 6.14, we obtain

$$F = 2\alpha G b^2 \frac{r}{r_c} \quad (6.16)$$

where α is a constant which depends on the nature of the dislocations [23], G is the shear modulus and r and r_c are the average radius and critical radius of the Al_3Sc precipitates respectively. The effective mean particle spacing, L , of the precipitates can be obtained by [64]:

$$L = \left(\frac{2\pi}{3f} \right)^{1/2} r \quad (6.17)$$

where f is the volume fraction of the precipitates. Therefore by substituting equation 6.16 and 6.17 into 6.13, the yield strength increment due to precipitates can be expressed in terms of the critical radius and the volume fraction:

$$\begin{aligned} \sigma_{ppt} &= \frac{M}{b} \frac{2\alpha G b (3f)^{1/2}}{r_c (2\pi)^{1/2}} \\ &= \frac{2.44 M \alpha G b}{\pi^{1/2} r_c} f^{1/2} \end{aligned} \quad (6.18)$$

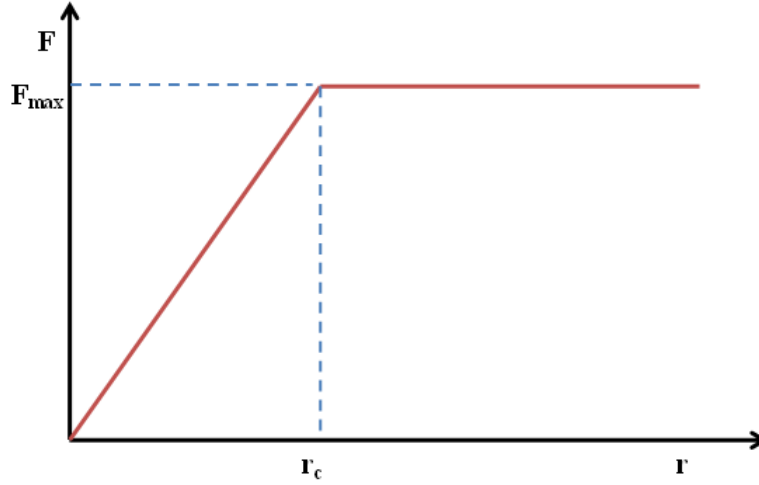


Figure 6.10: Schematic of interaction of a dislocation with a precipitate. r_c in this figure indicates the shearable to non-shearable transition for the precipitate. Above this radius, the force exerted by the dislocation reaches a maximum and the dislocation loops around the particle. Below this radius, the dislocation shears the particle.

In the present case, the yield strength of the Sc alloy during aging at 300 and 400°C can be estimated using the correlation of hardness and tensile results shown in Figure 6.1. Once, the yield strength is calculated, the incremental increase in yield strength up to peak strength can also be determined. As discussed previously, this increase in strength up to the peak-aged condition is attributed to the precipitation of Al_3Sc . Therefore it can also be represented by $\Delta\sigma_{ppt}$. Equation 6.18 can therefore be rewritten as:

$$\Delta\sigma_{ppt} = \frac{M}{b} \frac{2\alpha Gb(3f)^{1/2}}{r_c(2\pi)^{1/2}} = \frac{2.44M\alpha Gb}{\pi^{1/2}r_c} f^{1/2} \quad (6.19)$$

Figures 6.11 and 6.12 show the estimated change in yield strength ($\Delta\sigma_{ppt}$), plotted against the volume fraction and the square root of the volume frac-

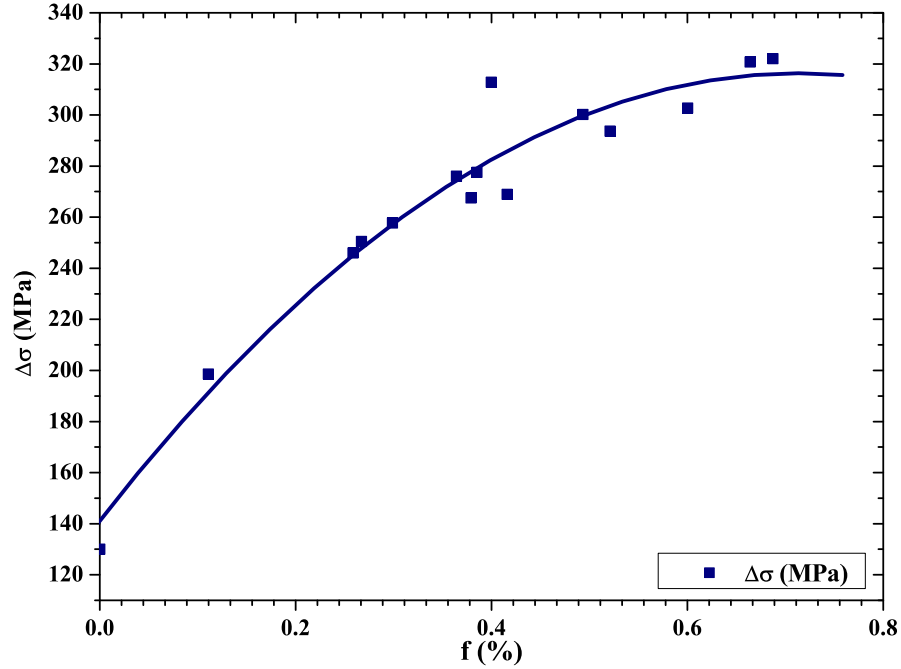


Figure 6.11: This plot shows the estimated yield strength at 300 and 400°C, determined by the correlation of the tensile and hardness data, plotted against the volume fraction of the Al_3Sc precipitates. The volume fraction is determined using the resistivity measurements. See equation 6.12.

tion ($f^{1/2}$), respectively, calculated using equation 6.12. Assuming that all the Sc atoms are in the precipitates, the maximum volume fraction of Al_3Sc particles would be $f_{Al_3Sc} = 0.93\%$. As can be seen in Figure 6.11, the volume fraction of the precipitates at peak-aged condition at 400°C has reached approximately 0.7%.

Finally, solving equation 6.19 for r_c , and using the slope of the curve shown in Figure 6.12, an estimated value of average radius of the Al_3Sc precipitates

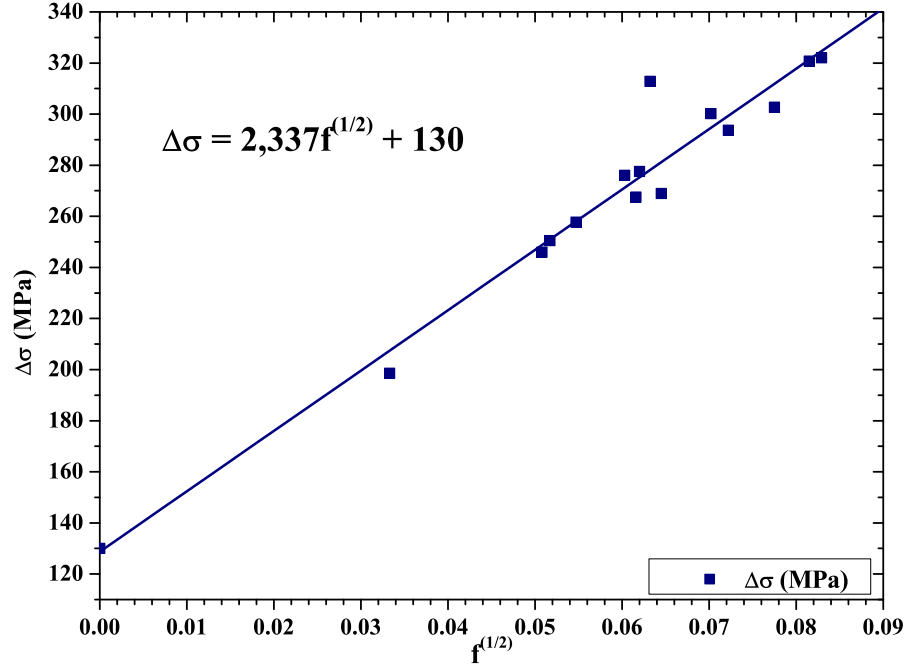


Figure 6.12: This plot shows the estimated yield strength at 300 and 400°C, determined by the correlation of the tensile and hardness data, plotted against the square root of the volume fraction of the Al_3Sc precipitates. The volume fraction is determined using the resistivity measurements. See equation 6.12. $R^2 = 0.96$ for this fit.

at the shearable to non-shearable transition point can be calculated:

$$r_c \approx \frac{2.44M\alpha Gb}{\pi^{1/2} \times 2337 \times 10^6} \approx 3.8nm \quad (6.20)$$

Table 6.3 summarizes the values used for the constants in the above equation.

As mentioned in the literature review in chapter 2, previous values reported

Table 6.3: Values of constants used in equation 6.18 [23]

Constant	α	M	G (GPa)	b (nm)
Value	0.27	3.06	27	0.286

for the shearable to non-shearable transition range from 2-3.7nm [21–23] indicating that $r_c = 3.8nm$ from present work is a reasonable estimation.

6.4 Summary

The response of the two alloys during heat treatments was found to be dependent on the precipitation of Al_6Mn and Al_3Sc and/or $Al_3(Sc_x, Zr_{1-x})$ phases and, in the CR case, the interaction of these precipitates with the deformed microstructure. The response of the base alloy was attributed to Mn precipitation in the form of Al_6Mn particles. The precipitation of Al_6Mn in the undeformed base alloy did not show any contribution to hardness. Furthermore, due to the slow diffusivity of Mn in Al, Mn precipitation had not reached equilibrium after 72 hours of aging at 400°C. This was shown by electrical resistivity measurements where the contribution of Mn to the change in resistivity of the alloy was determined using resistivity coefficients. Over the same aging period, however, a larger amount of Mn had precipitated out of solid solution in the cold rolled alloy. It was deduced that the high dislocation density in the deformed microstructure enhanced Mn precipitation. These precipitates were $\approx 100nm$ in size and were observed to be effective at inhibiting recrystallization provided the recrystallization kinetics were slower than precipitation kinetics. This was the case during aging at 300°C for 72 hours where a recovered but unrecrystallized microstructure

was observed in the base alloy. At 400°C however, the faster recrystallization kinetics allowed for recrystallization to occur prior to the formation of a significant amount of Mn-containing particles. Therefore the precipitation of Mn is affected by the dislocation density and in turn recovery and recrystallization processes are also affected by the Mn-containing precipitates.

The response of the Sc alloy was shown to be a combination of Sc and Mn precipitation. In this case, both Al_6Mn and Al_3Sc and/or $Al_3(Sc_x, Zr_{1-x})$ phases had formed. A strong precipitation hardening response was observed in hardness measurements during aging which was attributed to the formation of $Al_3(Sc_x, Zr_{1-x})$ precipitates. These precipitates were approximately 1-10nm in size and showed high stability as they remained coherent after aging for 72 hours at 400°C. In the AC case, the effect of Sc was isolated by assuming that the same Mn precipitation reaction occurs in the base alloy as in the Sc alloy. By subtracting the hardness and resistivity of the base alloy from those of the Sc alloy, the isolated response due to Sc precipitation was determined. It was shown that the hardness of the alloy increased by approximately 54VHN due to Sc precipitation during aging at 300°C.

Unlike Mn, however, the precipitation of Sc did not seem affected by the dislocation density in the microstructure. The calculation of the sum of the contributions of Sc and Mn to the change in resistivity of the Sc alloy was consistent with the measured change in resistivity during aging in both the AC and CR conditions. This calculation showed that the same amount of Sc precipitated during aging at 300°C as during 400°C. It was also shown that the majority of Sc precipitation occurs prior to Mn precipitation at both temperatures. The delay in Mn precipitation was attributed to the slower

diffusivity of Mn in Al relative to Sc in Al.

The complex interaction of Al_6Mn precipitates with the deformed microstructure made isolating the effect of Sc in the CR Sc alloy challenging and difficult to model.

The highest yield and tensile strength for the Sc alloy were 384MPa and 424MPa respectively which were obtained after 4 hours of aging at 300°C. These values were found to be higher than most of the values previously reported in literature for Al-Mg alloys with similar Mg and Sc levels [1]. As mentioned earlier in this chapter, similar strength levels reported in literature were obtained when a higher cooling rate ($\approx 100\text{K/s}$ or higher) was used during casting (ex. references [43, 44]). This is consistent with the present case since Twin Belt Casting (TBC) also uses cooling rates of approximately 100K/s. Therefore, one can conclude that the higher cooling rate is a major contributor to the higher strength of the alloy. Rapid solidification allows for maintaining Sc (and Mn) in solid solution during casting which allows for maximizing the precipitation hardening effect of the Al_3Sc phase. Furthermore, with TBC, this effect can be obtained by a two step process: cold rolling followed by annealing which is industrially advantageous since the homogenization is eliminated. This makes TBC an attractive process for fabricating Al-Mg alloys with Sc and Zr additions.

Chapter 7

Concluding Remarks and Perspectives

7.1 Conclusions

The aging behavior of two Twin Belt Cast AlMgMnZr alloys, one Sc-free and the other with 0.4%Sc addition, was investigated in the AC and CR conditions. The response of the two alloys were compared through hardness and tensile tests tests and resistivity measurements.

The Sc-containing alloy showed a strong aging response while a steady softening response was observed in the base alloy. The response of the base alloy was dominated by Al_6Mn precipitation. Precipitation of Mn however was shown to be strongly influenced by the deformed microstructure and vice versa. On the other hand, the response of the Sc alloy was a combination of Al_3Sc and/or $Al_3(Sc_x, Zr_{1-x})$ as well as Al_6Mn precipitation. In this case however, the Al_3Sc particles were shown to have a remarkable effect on the

retention of the deformed microstructure during aging.

The yield, tensile strength and uniform elongation of the Sc alloy were determined to be 384, 423MPa and 6% respectively at the peak aged condition. These values were superior to those typically reported for AlMg alloys with similar Mg and Sc contents. Comparable values reported in literature were consistently found to be attributed to alloys cast with rapid solidification rates. This confirms that the high cooling rates used in TBC are sufficient for retention of Sc (and Mn) in solid solution during casting. This supersaturation then allows for efficient precipitation of the Al_3Sc phase. Furthermore, the TBC process eliminates the homogenization step which is industrially advantageous. This makes TBC a particularly attractive technique for fabrication of AlMg alloys with Sc and Zr additions.

7.2 Future Recommendations

- In this investigation, it was determined that fine Al_6Mn precipitates which formed during aging, effected the recovery behavior of the base alloy. These precipitates were however ineffective at enhancing the hardness of the alloy if formed after recrystallization has occurred (ex. aging at 400°C). Furthermore, as was shown in the CR Sc alloy, the combined effect of Mn and Sc makes an especially complex situation where the interaction of the precipitates with each other and the deformed microstructure is difficult to quantify. It may therefore be beneficial for comparison purposes, to TBC an alloy with no Mn and similar remaining compositions to the base and Sc alloys.

- As noted, in the previous chapter, the role of Zr was also unquantifiable in this investigation. Due to the small size of the precipitates, EDX analysis of the $Al_3(Sc, Zr)$ particles was proven difficult. It was therefore, not possible to confirm if these particles do in fact exhibit a core-shell structure as described in the literature. As also noted previously, the diffusivity of Zr is also about 10,000 times lower than that of Sc in Al ($6.3 \times 10^{-24} m^2/s$ for Zr and $9.0 \times 10^{-20} m^2/s$ for Sc at $300^\circ C$). Therefore, it is possible that little Zr would have diffused out of solid solution to form around the Al_3Sc particles during aging at 200 or $300^\circ C$. At $400^\circ C$, however the diffusivity of Zr is only about 1000 times slower than that of Sc and therefore core-shell particles may have formed. This would also explain the slow coarsening of the precipitates at this temperature. Hence it is recommended that the precipitates in the Sc alloy aged at $400^\circ C$ for 72 hours, be further examined with high resolution transmission electron microscopy (HRTEM) in order to determine the nature of these precipitates and examine the role of Zr in particle coarsening in more detail.
- As mentioned in Chapter 1, the high cost of Sc (\$163/gram for 99.9% pure ingot and \$220/kg for Al-2%Sc master alloy [3]), limits the potential application of AlMgSc alloys to the aerospace industry. However, as shown in the reviewed investigations as well as the present work, less than 0.4%Sc is required in order to reach the high strengths observed. In the particular case of the TBC Sc alloy, it was shown that approximately 20% of the Sc added to the alloy was lost to the large primary

constituents in the AC microstructure. Through improvements of the casting process, the formation of these large constituents may be eliminated and therefore the Sc content can be reduced by at least 20%. It would therefore be also valuable to explore the properties of alloys with various levels of Mg and Sc. Lowering the Sc content may mean sacrificing the grain refinement achieved in the AC structure due to Sc. On the other hand, if a combination of high strength and good ductility are found in Al-Mg alloys with lower Sc content, the cost of the alloy would be reduced which would further expand the areas in which this alloy may be applied.

Bibliography

- [1] Royset, J. and Ryum, N. *International Materials Reviews* **50**(1), 19–44 (2005). → pages 1, 2, 3, 5, 6, 7, 8, 9, 10, 11, 12, 13, 14, 17, 65, 83, 95
- [2] Fuller, C. B. *Temporal Evolution of the Microstructures of Al(Sc,Zr) Alloys and Their Influences on Mechanical Properties*. PhD thesis, Northwestern University, (2003). → pages 2, 3, 6, 7, 13, 18, 55
- [3] Cordier, D. J. Summary, U.S. Geological Survey, January (2012). → pages 3, 98
- [4] Gallerneault, M. October (2007). → pages 3, 19, 20, 21, 22
- [5] Davydov, V., Rostova, T., Zakharov, V., Filatov, Y., and Yelagin, V. *Materials Science and Engineering: A* **280**(1), 30–36 March (2000). → pages 3, 18
- [6] Kaiser, M. S., Datta, S., Roychowdhury, A., and Banerjee, M. K. *Materials and Manufacturing Processes* **23**(1), 74–81 (2007). → pages
- [7] Lathabai, S. and Lloyd, P. *Acta Materialia* **50**(17), 4275–4292 October (2002). → pages 3, 18
- [8] Burrell, A. W. L. and Burrell, A. W. L. November (1971). U.S. Classification: 420/538. → pages 6, 9, 10, 11, 16
- [9] Toropova, L. S., Eskin, D. G., Kharakterova, M. L., and Dobatkina, T. V. *Advanced Aluminum Alloys Containing Scandium: Structure and Properties*. Taylor & Francis, June (1998). → pages 6
- [10] Hyland, R. *Metallurgical and Materials Transactions A* **23**(7), 1947–1955 July (1992). → pages 6, 7, 8

- [11] Marquis, E. A. *Microstructural Evolution and Strengthening Mechanisms in Al-Sc and Al-Mg-Sc Alloys*. PhD thesis, Northwestern University, (2002). → pages 6, 7, 10, 14, 15, 87
- [12] Marquis, E. and Seidman, D. *Acta Materialia* **49**(11), 1909–1919 June (2001). WOS:000169312500004. → pages 7, 8
- [13] Tsivoulas, D. and Robson, J. D. In *Aluminium Alloys 2006, Pts 1 and 2: Research Through Innovation and Technology*, Poole, W., Wells, M., and Lloyd, D., editors, volume 519-521, 473–478. Trans Tech Publications Ltd, Zurich-Uetikon (2006). WOS:000240309000071. → pages 8
- [14] Johansen, A. *MICROSTRUCTURES AND PROPERTIES OF ALUMINIUMMAGNESIUM ALLOYS WITH ADDITIONS OF MANGANESE, ZIRCONIUM AND SCANDIUM*. Doktor ingenir dissertation, The Norwegian University of Science and Technology (NTNU), (2000). → pages 8, 13, 75, 78, 83
- [15] Ferry, M., Hamilton, N., and Humphreys, F. *Acta Materialia* **53**(4), 1097–1109 February (2005). → pages 8
- [16] YE, Y.-c., HE, L.-j., and LI, P.-j. *Transactions of Nonferrous Metals Society of China* **20**(3), 465–470 March (2010). → pages 8
- [17] Norman, A. F., Prangnell, P. B., and MEwen, R. S. *Acta Materialia* **46**(16), 5715–5732 October (1998). → pages 9
- [18] Liu, Z., Li, Z., Wang, M., and Weng, Y. *Materials Science and Engineering: A* **483484**(0), 120–122 June (2008). → pages 9
- [19] Jones, M. J. and Humphreys, F. J. *Acta Materialia* **51**(8), 2149–2159 May (2003). → pages 9
- [20] Riddle, Y. W. and Sanders, T. H. J. *Materials Science Forum* **331-337**, 799–804 (2000). → pages 9
- [21] Seidman, D. N., Marquis, E. A., and Dunand, D. C. *Acta Materialia* **50**(16), 4021–4035 September (2002). → pages 11, 93
- [22] Fuller, C. B., Seidman, D. N., and Dunand, D. C. *Acta Materialia* **51**(16), 4803–4814 September (2003). → pages 11, 13

-
- [23] Fazeli, F., Poole, W. J., and Sinclair, C. W. *Acta Materialia* **56**(9), 1909–1918 May (2008). WOS:000256140800001. → pages 11, 12, 16, 88, 89, 93
- [24] Ryset, J., Ryum, N., Bettella, D., Tocco, A., Jia, Z., Solberg, J. K., and Reiso, O. *Materials Science and Engineering: A* **483484**(0), 175–178 June (2008). → pages 12
- [25] Roumina, R. and Sinclair, C. *Metallurgical and Materials Transactions A* **42**(2), 473–487 February (2011). → pages 12
- [26] Fuller, C. B. *Temporal Evolution of the Microstructures of Al(Sc,Zr) Alloys and Their Influences on Mechanical Properties*. PhD thesis, NORTHWESTERN UNIVERSITY, EVANSTON, ILLINOIS, (2003). → pages 13, 14
- [27] Deschamps, A., Lae, L., and Guyot, P. *Acta Materialia* **55**(8), 2775–2783 May (2007). → pages 13
- [28] Knipling, K. E., Karnesky, R. A., Lee, C. P., Dunand, D. C., and Seidman, D. N. *Acta Materialia* **58**(15), 5184–5195 September (2010). → pages 13, 14
- [29] Knipling, K. E., Seidman, D. N., and Dunand, D. C. *Acta Materialia* **59**(3), 943–954 February (2011). WOS:000286690100009. → pages 13, 70
- [30] Lohar, A., Mondal, B., Rafaja, D., Klemm, V., and Panigrahi, S. *Materials Characterization* **60**(11), 1387–1394 November (2009). → pages 14
- [31] Song, M., He, Y., and Fang, S. *Journal of Materials Engineering and Performance* **20**(3), 377–381 June (2010). → pages 14
- [32] Kendig, K. and Miracle, D. *Acta Materialia* **50**(16), 4165–4175 September (2002). → pages 14, 18
- [33] Riddle, Y. and Sanders, T. *Metallurgical and Materials Transactions A* **35**(1), 341–350 January (2004). → pages 14
- [34] Associates, J. D. . and Committee, A. I. H. *Aluminum and Aluminum Alloys*. ASM International, (1993). → pages 15, 50
- [35] Marquis, E. A. and Seidman, D. N. *Acta Materialia* **53**(15), 4259–4268 September (2005). → pages 15, 16

- [36] Kaiser, M., Datta, S., Roychowdhury, A., and Banerjee, M. *Journal of Materials Engineering and Performance* **17**(6), 902–907 December (2008). → pages 16
- [37] Deschamps, A. and Brechet, Y. *Acta Materialia* **47**(1), 293–305 December (1998). WOS:000077996000028. → pages 16
- [38] Robson, J. D., Jones, M. J., and Prangnell, P. B. *Acta Materialia* **51**(5), 1453–1468 March (2003). WOS:000181677700021. → pages 16
- [39] Ocenasek, V. and Slamova, M. *Materials Characterization* **47**(2), 157–162 August (2001). WOS:000172928100010. → pages 17
- [40] Fuller, C. B., Krause, A. R., Dunand, D. C., and Seidman, D. N. *Materials Science and Engineering A* **338**(1-2), 8–16 December (2002). → pages 17, 65
- [41] Filatov, Y., Yelagin, V., and Zakharov, V. *Materials Science and Engineering: A* **280**(1), 97–101 March (2000). → pages 17
- [42] Herding, T., Keler, O., and Zoch, H. w. *Materialwissenschaft und Werkstofftechnik* **38**(10), 855–861 October (2007). → pages 18
- [43] Sawtell, R. and Jensen, C. *Metallurgical and Materials Transactions A* **21**(1), 421–430 January (1990). → pages 18, 65, 95
- [44] PARKER, B., ZHOU, Z., and NOLLE, P. *Journal of Materials Science* **30**(2), 452–458 January (1995). WOS:A1995QE93800024. → pages 18, 65, 95
- [45] Sanders, R. E. *Jom* **64**(2), 291–301 February (2012). WOS:000301040000017. → pages 18, 19
- [46] Sanders, R. E. *JOM* **53**(2), 21–25 (2001). → pages 18, 19
- [47] Gallerneault, M. and Lloyd, D. J. *Materials Science Forum* **396-402**, 95–100 (2002). → pages 19, 20, 21
- [48] Sarkar, S. <https://circle.ubc.ca/handle/2429/14667>, November (2003). → pages 19, 21, 22
- [49] Girard, S. X., Azari, H. N., and Wilkinson, D. S. *Metallurgical and Materials Transactions A* **35**(3), 949–952 March (2004). → pages

-
- [50] Zhao, P. Z., Anami, T., Okamoto, I., Mizushima, K., Gatenby, K. M., Gallerneault, M., Barker, S., Yasunaga, K., Goto, A., Kazama, H., and Hayashi, N. *Development of twin-belt cast AA5XXX series aluminum alloy materials for automotive sheet applications*. Minerals, Metals & Materials Soc, Warrendale, (2009). WOS:000263684500002. → pages 22, 24
- [51] Sarkar, S., Wells, M., and Poole, W. *Materials Science and Engineering: A* **421**(12), 276–285 April (2006). → pages 23, 70, 72
- [52] Manning, T. J. and Grow, W. R. *The Chemical Educator* **2**(1) (1997). → pages 28
- [53] Halim, H., Wilkinson, D. S., and Niewczas, M. *Acta Materialia* **55**(12), 4151–4160 July (2007). WOS:000247980200009. → pages 36
- [54] Kang, D. H., Sohi, M., Mousavi Anijdan, H., Singh, N., and Gallerneault, M. In *13th International Conference on Aluminum Alloys (ICAA13)* (, Pittsburgh, Pennsylvania, 2012). → pages 55
- [55] Ashby, M. and Brown, L. *Philosophical Magazine* **8**(91), 1083–& (1963). WOS:A19631401C00002. → pages 59
- [56] Roumina, R. *MECHANICAL PROPERTIES OF A RECOVERED Al-Mg-Sc ALLOY*. PhD thesis, University of British Columbia, Vancouver, BC, March (2009). → pages 59
- [57] Cahoon, J., Broughton, W., and Kutzak, A. *Metallurgical and Materials Transactions B* **2**(7), 1979–1983 (1971). → pages 66
- [58] Raeisinia, B. and Poole, W. J. In *Aluminium Alloys 2006, Pts 1 and 2: Research Through Innovation and Technology*, Poole, W., Wells, M., and Lloyd, D., editors, volume 519-521, 1391–1396. Trans Tech Publications Ltd, Zurich-Uetikon (2006). WOS:000240309000221. → pages 70, 71
- [59] Raeisinia, B., Poole, W., and Lloyd, D. *Materials Science and Engineering: A* **420**(12), 245–249 March (2006). → pages 72, 87
- [60] Davis, J. R. *Aluminum and Aluminum Alloys*. ASM International, (1993). → pages 73, 75
- [61] Hatch, J. E., Association, A., and Metals, A. S. f. *Aluminum: properties and physical metallurgy*. ASM International, (1984). → pages 73, 74, 76

- [62] Hansen, V., Andersson, B., Tibballs, J., and Gjnnes, J. *Metallurgical and Materials Transactions B* **26**(4), 839–849 (1995). → pages 80
- [63] Vlach, M., Stulikova, I., Smola, B., Piesova, J., Cisarova, H., Danis, S., Plasek, J., Gemma, R., Tanprayoon, D., and Neubert, V. *Materials Science and Engineering: A* **548**(0), 27–32 June (2012). → pages 80
- [64] Ardell, A. *Metallurgical and Materials Transactions A* **16**(12), 2131–2165 (1985). → pages 89